Control of the single atom/nanoparticle ratio in Pd/C catalysts to optimize the cooperative hydrogenation of alkenes

Camila Rivera-cárcamo, I.C. Gerber, Iker Del rosal, B. Guicheret, Rubén Castro Contreras, L. Vanoye, A. Favre-Reguillon, Bruno F Machado, J. Audevard, C. de Bellefon, et al.

Control of the single atom/nanoparticle ratio in Pd/C catalysts to optimize the cooperative hydrogenation of alkenes

Received 00th January 20xx,
Accepted 00th January 20xx

DOI: 10.1039/x0xx00000x

C. Rivera-Cárcamo,[a] I. C. Gerber,[b,*] I. del Rosal,[b] B. Guicheret,[c] R. Castro Contreras,[a] L. Vanoye,[c] A. Favre-Réguillon,[c,d] B. F. Machado,[e] J. Audevard,[a] C. de Bellefon,[c] R. Philippe[c,*] and P. Serp[a,*]

We recently reported (*J. Catal., 2019, 372, 226-244*) that a structure/activity correlation exists in Pd/C catalysts for myrcene hydrogenation, which integrates the Pd dispersion, and the surface concentration of oxygen groups and defects of the support. Here, through a combined experimental-theoretical study, we provide an explanation of the influence of these three structural characteristics of Pd/C catalysts for alkene hydrogenation. Highly dispersed Pd nanoparticles (Pd_{NP}) are necessary to activate dihydrogen. A high concentration of surface defects on the support is necessary to stabilize Pd single atoms (Pd_{SA}), which coexist with Pd_{NP} on Pd/C catalysts. A high concentration of oxygenated surface groups is also necessary on the support to allow hydrogen spillover. We demonstrate that such combination allows a cooperative catalysis to operate between Pd_{NP} and Pd_{SA} that involves the formation of Pd_{SA}-H species, which are much more active than Pd_{NP}-H for alkene hydrogenation but also isomerization. Importantly, we also report an efficient method to control the ratio between Pd_{SA} and Pd_{NP} in Pd/C catalysts of similar loadings and show that the control of this ratio allows the development of a new generation of stable and highly active catalysts integrating the ultra-rational use of precious metals in short supply. Indeed, for myrcene hydrogenation activity variations of several orders of magnitude were measured as a function of the value of this ratio.

1. Introduction

The hydrogenation of alkenes is among the important technological reactions catalyzed by supported metals, finding application in the pharmaceutical, agrochemical, refining, and commodity chemical industries. As the catalyst active phase is often made of noble metals, expensive and for the most part identified as critical elements, a logical step is to optimize their dispersion on the support.[1] The highest dispersion that can be achieved corresponds to supported isolated metal atoms. Supported single-atoms (SA) have coexisted with metal nanoparticles (NP) for a long time,[2] and may have played significant roles in many catalytic processes, but they have rarely been recognized as active sites. Today, aided by recent advances in synthesis methodologies, characterization techniques and computational modelling, single-atom catalysis has decidedly become the most active new frontier in heterogeneous catalysis.[3] Single atoms exhibit distinctive performances from the ones of NP for a wide variety of chemical reactions, and industrial applications employing them already exist.[4] The absence of atomic ensemble effects, and the charge transfer to or from the support, that strongly modifies the electronic structure of the metal atom in SA catalysts, significantly affect the adsorption, and definitively induce a different reactivity compared to metallic NP.[5] Current studies conducted on SA catalysts focus mainly on distinguishing them from NP and the possibility of synergy between these two species have been rarely explored.[6-11] Interestingly, it was proposed that a synergy may operate between Pd_{SA} and Pd_{NP} during ketone/aldehyde hydrogenation on Pd/TiO_2 catalysts.[7] In this reaction, Pd_{SA} contributes for the C=O activation while Pd_{NP} allow the easy dissociation of H_2.

Palladium on carbon is a very common catalyst for alkene hydrogenation.[12] Hydrogenations with Pd_{SA} have been already reported,[3,13] but the metal-support interaction in such catalysts often results in an ionic/electron-deficient state of the metallic atoms that prevents an efficient H_2 activation compared to metallic surfaces,[7,13-15] and limits their application to specific selective hydrogenation reactions.[16,17] Although a direct H_2 activation has been reported for Pd/Cu single-atom alloy,[16] on Pd_{SA}, H_2 activation is performed thanks to support-assisted molecular hydrogen heterolytic dissociation.[18,19] Given that H_2 dissociation is often the rate-limiting step in these reactions, efficient strategies toward engineering the minimal catalytic ensemble that can activate H_2 would represent a substantial progress in pursuit of highly efficient Pd/C hydrogenation catalysts.

Here, through a combined experimental-theoretical study, we show that for alkene (myrcene, squalene, farnesene) hydrogenation a cooperative catalysis takes place between carbon-supported Pd_{SA} and Pd_{NP}. First, Pd_{NP} dissociate H_2 easily, and subsequent hydrogen spillover provides Pd-H species on Pd_{SA} (H-Pd_{SA}). The H-Pd_{SA} are much more active than H-Pd_{NP} for the hydrogenation and isomerization of C=C double bonds. Thanks to the control of the SA/NP ratio on the support, which has been achieved in this work, the rational design of highly active catalysts becomes possible.

[a] *LCC-CNRS, Université de Toulouse, UPR 8241 CNRS, INPT, Toulouse, France*
[b] *LPCNO, Université de Toulouse, CNRS, INSA, UPS, 135 avenue de Rangueil, F-31077 Toulouse, France*
[c] *LGPC, Université de Lyon, UMR 5285 CNRS, CPE Lyon, Université Claude Bernard Lyon, France*
[d] *Conservatoire National des Arts et Métiers, UPN7-CG, 2 rue Conté, F-75003 Paris, France*
[e] *Laboratory of Separation and Reaction Engineering - Laboratory of Catalysis and Materials (LSRE-LCM), University of Porto, Rua Dr. Roberto Frias s/n, 4200-465 Porto, Portugal*
*Correspondence to: igerber@insa-toulouse.fr; rph@lgpc.cpe.fr; philippe.serp@ensiacet.fr.
Electronic Supplementary Information (ESI) available: [Materials, Catalytic experiments, Tests to assess hydrogen spillover, Assessment of the impact of mass transfer for myrcene hydrogenation, Figs. S1 to S16].

2. Materials and methods

Palladium catalyst synthesis

A wet impregnation method was used to prepare the palladium catalysts supported on carbon nanomaterials. The desired amount of palladium(II) nitrate dihydrate [$Pd(NO_3)_2{\cdot}2H_2O$] (Sigma-Aldrich) was added to acetone (100 mL) containing 1 g of carbon nanomaterial, so as to introduce 2 %w/w of metal phase. The solution was sonicated at room temperature for 1 h and magnetically stirred overnight. The solution was then filtered and washed with acetone. The resulting solid was dried in an oven at 120 °C overnight. Finally, the 2% Pd/CNT catalyst was reduced in a horizontal tube oven under a nitrogen and hydrogen flow (20 vol% H_2) at 300 °C for 2 h (25°C to 300 °C at 10 °C/min). The same procedure was followed for the 1.6% Pd/CNT_{HT}, by using the CNT_{HT} support.

For Pd_{SA} synthesis (0.1% Pd_{SA}/CNT), the wet impregnation method was also used. The desired amount of palladium(II) nitrate dihydrate [$Pd(NO_3)_2{\cdot}2H_2O$] was added to an acetone solution (100 mL) containing 1 g of CNT_{ox}, so as to introduce 0.1 %w/w of metal phase. The solution was sonicated at room temperature for 6 h using an ultrasonic finger. The solution was then filtered and washed with acetone. The resulting solid was dried in an oven at 120 °C overnight. Finally, the catalyst was reduced in a horizontal tube oven under a nitrogen and hydrogen flow (20 vol% H_2) at 300 °C for 2 h (25°C to 300°C at 10°C/min).

For $Pd_{X\_SA/NP}$/CNT catalysts synthesis where X refers to SA/NP ratio, a recently patented process was used.[20] The process consists in: i) creating carboxylic groups on the support by nitric acid oxidation (step I); ii) decomposing these groups under an inert atmosphere to produce CO_2, some H_2 and carbon vacancies (step II); and iii) depositing the metal on this defective support (step III). For a given metal loading, if step III is performed once, only Pd_{SA} are obtained; and if it is performed several times, mixtures of SA and NP are obtained. The number of times that step III is performed for a given total metal loading, conditions the SA/NP ratio. For $Pd_{X\_SA/NP}$/CNT catalysts on D-CNT the desired amount of bis(2-methylallyl)palladium precursor (Nanomeps) was added under argon to a pentane solution of D-CNT. At the end of each cycle the catalyst was treated under a nitrogen and hydrogen flow (20 vol% H_2) at 80 °C for 1 h.

Finally, a 0.1%$Pd_{1000\_SA/NP}$ with a SA/NP ratio > 1000 was also prepared by the wet impregnation method. The desired amount of palladium(II) nitrate dihydrate [$Pd(NO_3)_2{\cdot}2H_2O$] was added to an acetone solution (100 mL) containing 1 g of CNT_{ox}, so as to introduce 0.1 %w/w of metal phase. The solution was sonicated at room temperature for 1 h. Then, $NaBH_4$ (0.1 g) was added at room temperature, and let to react for 1 h to complete catalyst reduction. The solution was then filtered and washed with water and then acetone. The resulting solid was dried in an oven at 120 °C overnight.

For comparison purpose in myrcene hydrogenation we also used a commercial 5%Pd/activated carbon catalyst and a 5%Pd/Al_2O_3 catalyst. The Table S1 presents the different catalysts used in this study.

Characterization

The palladium content in the products was measured by inductively coupled plasma optical emission spectroscopy (ICP-OES) performed at the LCC with a Thermo Scientific ICAP 6300 instrument. Elemental analyses of C, H were carried out on a PERKIN ELMER 2400 serie II elemental analyzer. TEM and HR-TEM analyses were performed at the "Centre de microcaracterisation Raimond Castaing, UMS 3623, Toulouse" by using a JEOL JEM 1011 CX-T electron microscope operating at 100 kV with a point resolution of 4.5 Å and a JEOL JEM 1400 electron microscope operating at 120 kV. The high-resolution analyses were conducted by using a JEOL JEM 2100F equipped with a field emission gun (FEG) operating at 200 kV with a point resolution of 2.3 Å and a JEOL JEM-ARM200F Cold FEG operating at 200 kV with a point resolution of > 1.9 Å. The particle size distribution was determined through a manual measurement of enlarged micrographs from different areas of the TEM grid (at least 300 particles).

The size distribution reported as Pd atomic percentage (based on total atoms) in each size range were obtained by calculating the number of atoms (N) in each nanoparticle assuming a spherical shape using an equation described in.[21] The SA/NP ratio (a number ratio) was measured from the STEM-HAADF analyses of at least 500 elements.

The samples were analyzed by X-ray photoelectron spectroscopy (XPS) using a VG Escalab MKII spectrophotometer operating with a non monochromatized Mg K source (1253.6 eV). A SQuID magnetometer MPMS5 was used to investigate the magnetic properties. The M(H) loop was measured at T = 300 K after cooling the sample from 300 K to 2 K under a constant applied magnetic field H_{cool} = 50 kOe. The M(H) loops were measured between -50 and 50 kOe. EPR data were recorded using an Elexsys E 500 Bruker spectrometer, operating at a microwave frequency of approximately 9.5 GHz. All spectra were recorded using a microwave power of 20 mW across a sweep width of 150 mT (centered at 310 mT) with modulation amplitude of 0.5 mT. Experiments were carried out at 110 K using a liquid nitrogen cryostat.

DFT periodic calculations

Calculations using periodic boundary conditions were performed using the Vienna *ab initio* simulation package VASP,[22-25] which employs the full-potential projector augmented waves (PAW) framework.[26,27] Exchange-correlation effects were approximated using the PBE functional and applied in spin-polarized calculations.[28] A kinetic energy cutoff of 400 eV was found to be sufficient to achieve a total energy convergence within several meV, considering k-point sampling, i.e. with a (3x3x1) Γ-centered grid in conjunction with a 0.05 eV-width Gaussian smearing. All atoms were fully relaxed in order to have forces smaller than 0.005 eV/$Å^{-1}$, and the Nudged Elastic Band method was used to estimate minimum energy paths of transitions, as implemented by Henkelman *et al.*,[29,30] using 3 intermediates images and force criteria of 0.05 eV/$Å^{-1}$ to control the convergence. We have modeled the carbon support by a single graphene layer presenting a

vacancy in (7x7) supercell, which can be either filled by a single Pd atom (Pd_{SA}-model) or served as an anchorage point for a fully hydrogenated $Pd_{13}H_{20}$ aggregate (Pd_{NP}-model). We recall that a sufficient vacuum height of 16 Å was used to limit spurious interaction between repeated images in the z-direction due to periodic boundary conditions.

DFT Gaussian calculations

Calculations were carried out using the Gaussian09 package[31] at the DFT level by means of the hybrid density functional B3PW91.[32,33] For the Pd atom, the Stuttgart-Dresden pseudopotentials[34] were used in combination with their associated basis sets[35] augmented by a set of polarization functions (f-orbital polarization exponents of 1.472).[36] For the C and H atoms, a double-zeta 6-31G basis set[37-43] augmented by a polarization function were used. The different intermediates and transition states were simulated with dispersion corrected functional. More precisely, dispersion corrections were treated with the D3 version of Grimme's dispersion with Becke-Johnson damping.[44] The nature of the optimized stationary point, minimum or transition state, has been verified by means of analytical frequency calculations at 298.15 K and 1 atm. The geometry optimizations have been achieved without any geometrical constraints. IRC calculations were carried out to confirm the connectivity between reactant(s), transition state and product(s). Energy data in kcal/mol are reported in the gas phase.

Catalytic experiments

β-myrcene hydrogenation

Myrcene catalytic hydrogenation has been carried out in a stirred tank reactor of 200 mL from Top Industrie. This reactor is equipped with 4 baffles and a gas inducing Rushton turbine having 6 straight blades to provide an efficient G-L-S contacting. The catalytic tests were operated at 1200 rpm and 120 °C with 200 mg of catalyst powder (except for Pd/C and Pd/Al_2O_3 catalysts where 80 mg of catalyst has been used because of their Pd loading of 5 wt.%) under pure H_2 atmosphere at a constant pressure of 20 bar. The liquid phase consists in 80 mL of a 1M *β*-myrcene (Sigma-Aldrich, 98% purity, corresponding to 3M of C=C double bond) solution in n-heptane (Sigma-Aldrich, 99%) containing a known trace of n-tetradecane as internal standard for final GC-FID analysis (DB17 column). In this configuration, the reactor is operated in batch mode for the liquid and solid phases and in semi-batch mode for the gas because hydrogen was constantly fed *via* a pressure regulator and supplied by a calibrated reserve. The pressure and temperature monitoring of this reserve provides the hydrogen consumption rate, and thus the apparent and instantaneous activity of the catalysts expressed in moles of H_2 consumed per mole of Pd and per second, and being equivalent to an instantaneous Site Time Yield ("STY" in the following).

The instantaneous STY is determined with the local slope of the H_2 reserve consumption curve as following, where n_{Pd} is the quantity of Pd determined by ICP:

$$STY = \frac{\Delta n_{H_2}}{\Delta t \times n_{Pd}} \left(mol_{H_2}/mol_{Pd}/s\right)$$

STY is qualified of apparent because (i) it addresses the overall consumption of H_2 through multiple reactions and (ii) depending on the catalyst and the reaction progress, possible external and internal mass transfer resistances are likely. Indeed, the reactivity of the first C=C is very high (terminal and conjugated C=C) and the first moments of the reaction are physically limited. Hopefully, this is not true for the whole range of reaction course. For robust and chemically consistent catalysts comparison, STY at 66% and 83% of reaction progress are thus considered, *i.e.* when 2.0 and 2.5 equivalents of H_2 per *β*-myrcene are consumed respectively. More details about the characterization of possible internal and external mass transfer limitations throughout the reaction progress are available in the Supplementary Informations in the corresponding section S.4.

For a fair comparison with commercial catalysts, a STY* could be also used where n_{Pd} is replaced by S_{Pd}, the quantity of surface Pd determined from metal dispersion (Table S1)

$$STY^* = \frac{\Delta n_{H_2}}{\Delta t \times S_{Pd}} \left(mol_{H_2}/mol_{Pd}/s\right)$$

For hydrogenation and isomerization reactions, we have also used normalized time (time.cat), a standardized notation that is convenient and usual in catalysis to compare catalysts with different loadings of the active phase. The quantity of Pd was determined by ICP. For comparison with commercial catalysts (Fig. S1a), a time.cat* could be also used where n_{Pd} is replace by S_{Pd}, the quantity of surface Pd determined from metal dispersion (Table S1).

To ensure a reproducible and precise initial times for the tests, heating of the reactor was first done with 1 bar of N_2, then agitation was stopped and the N_2 atmosphere was replaced by 20 bar of H_2 and agitation turned on again, defining the initial time for the experiment. No side-reactions like Diels-Alder or oligomerization are encountered in the experimental domain investigated for this substrate. Thus, no selectivity issue has to be considered. The good matching between the evolution of H_2 consumption profiles and of liquid substrate compositions has been checked (not shown here) and validates the experimental approach for reaction progress monitoring.

Squalene and β-farnesene hydrogenation

The comparison between β-myrcene, β-farnesene and squalene hydrogenations have been carried out in the same experimental rig following the same procedure with identical experimental conditions excepting a slightly increased catalyst mass (280 mg instead of 200 mg). To illustrate the extension of the concept to other carbon supports, here FLG was chosen and compared to Al_2O_3. Squalene has been purchased from Sigma-Aldrich and *β*-farnesene has been synthesized and purified accordingly to ref.[45].

Catalyst stability testing under continuous reactor operation

Catalyst stability has been investigated through a dedicated continuous reactor operation with coated metallic open-cell solid foams (Hollomet Foamet 800 µm). Stainless steel foam cylinders were precisely cut through EDM (Electrical Discharge Machining) to obtain cylindrical objects with a diameter of 4.3 mm and a length of 5 cm. 8 foam pieces were homogeneously coated with 12.5 mg of the $Pd_{2\_SA/NP}$/CNT catalyst (following the detailed procedure described elsewhere[46]) and inserted into a home-made millimeter-scale tubular reactor (40 cm long, 4.4 mm I. D.) to provide a reactor volume of 6 mL with a total catalyst amount of 100 mg. Fig. S2 shows a photo of the foam coated in the tubular reactor. The continuous experiments were performed at 120 °C and 20 bar applying a gas flowrate of 2 NL/min of pure H_2 and a liquid flow rate of 2 mL/min of a 1M solution of myrcene in heptane corresponding to a liquid space velocity of 106.4 $mol_{myrcene}/mol_{Pd}$/min. Analysis by GC-FID (method and apparatus are identical to the one described in the previous β-myrcene hydrogenation section) at the reactor outlet allow to verify the mass balance and to determine the liquid flow composition. The corresponding mean Site Time Yield and Reaction progress are then calculated. It is noteworthy that this mean STY and the instantaneous STY used in the batch experiment are different and cannot be compared directly.

3. Results

Hydrogenation and isomerization of alkenes

As a model substrate *β*-myrcene, an acyclic polyunsaturated monoterpene with highly reactive 1,3-diene moiety, and an isolated tri-substituted C=C bond, was chosen (Fig. 1a). Complete hydrogenation to 2,6-dimethyloctane usually requires long reaction times, resulting in low average Site Time Yield (STY).[47] A comparison made between two commercial Pd/Al_2O_3 and Pd/C catalysts showed that the Pd/C catalyst is significantly more active (Fig. 1b,c). In order to exclude a possible influence of the microporosity of activated carbon, the same reaction was also performed on a Pd catalyst supported on carbon nanotubes (CNT), Pd/CNT showing comparable particle size with Pd/C (Supplementary Informations S1, Fig. S1, and Table S1). The catalytic activity of Pd/CNT and Pd/C are similar (Fig. 1b,c). Since the three catalysts present different Pd NP size, we also calculated the time.cat* and the STY* as a function of surface Pd (Fig. S3). A similar tendency was observed, *i.e.* higher STY* are obtained on the two carbon-supported catalysts. Analysis of these three catalysts by TEM and STEM-HAADF before and after reaction showed no very significant change in mean particle size after catalysis (Fig. S1). However, a major difference between these catalysts was the presence of Pd_{SA} on Pd/CNT and Pd/C (Fig. 2a-c). The probable presence of atomically dispersed Pd species on reduced Pd/CNT catalysts has been recently discussed by de Jong and coworkers.[1] For the Pd/CNT catalyst, a ratio SA/NP of 2 was measured and this catalyst will be named $Pd_{2\_SA/NP}$/CNT from now on (Fig. 2c). We independently checked that the SA/NP ratio of $Pd_{2\_SA/NP}$/CNT does not change after catalysis.

In parallel, mixtures of Pd_{SA} and Pd_{NP} were also obtained on other carbon supports such as few layer graphene or carbon nanofibers (Fig. S4). These latter catalysts are also very active compared to Pd/Al_2O_3 for the hydrogenation of various terpenes of industrial interest such as squalene or *β*-farnesene (Fig. S5). We also checked that for these catalysts the mean Pd_{NP} size and SA/NP ratio does not change significantly after catalysis (Fig. S6).

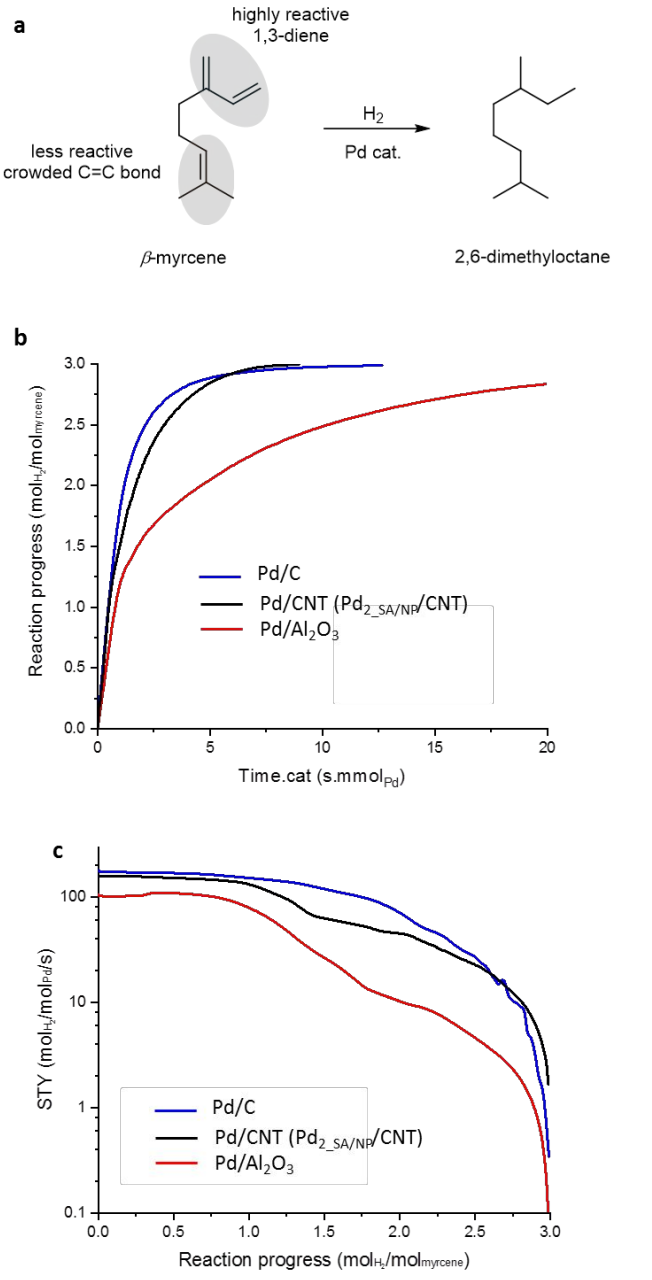

Figure 1. Catalytic results on Pd/Al_2O_3, Pd/C and Pd/CNT. **a** Myrcene hydrogenation reaction. The reaction was carried out over supported Pd catalysts. P_{H2} = 20 bar - T = 120°C - myrcene 1 M (80 mL) - solvent heptane - 4 mg Pd **b** Reaction progress as a function of time.cat. **c** STY as a function of reaction progress.

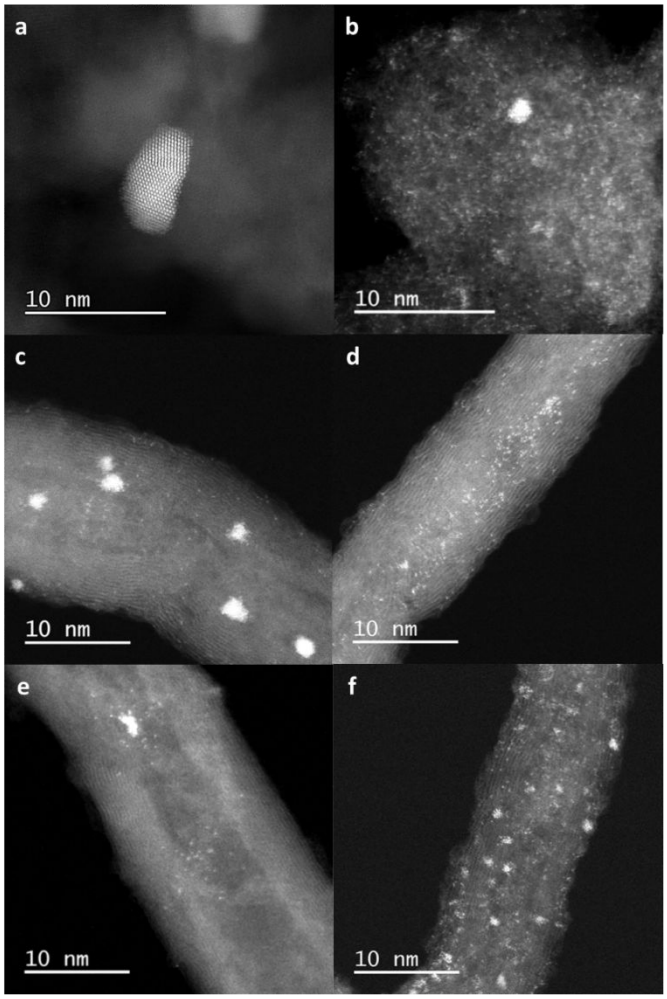

Figure 2. STEM-HAADF micrographs of: **a** Pd/Al_2O_3; **b** Pd/C; **c** $Pd_{2\_SA/NP}$/CNT; **d** Pd_{SA}/CNT; **e** $Pd_{2\_SA/NP}/CNT_{HT}$; and **f** $Pd_{10_SA/NP}$CNT catalysts. Scale bar = 10 nm.

The existence of Pd_{SA} on carbon supports can be attributed to the presence of specific anchoring sites such as structural defects, which are necessary for their stabilization.[13,48] From the reaction profiles of Fig. 1b,c, we can see that the reaction starts rapidly, then for Pd/Al_2O_3 it slows down, while a high rate is maintained for the catalysts supported on carbon. The rate decrease observed for the Pd/Al_2O_3 catalyst is probably associated to the difficult hydrogenation of the internal double bonds of myrcene.[49] In order to explain the stable activity of carbon supported catalysts, the possible involvement of acidic sites on these catalysts, which could assist the isomerization of the relatively crowded double bond to an easier to reduce one, has been investigated. Potentially, two types of acidic sites may coexist on the carbon-supported catalysts. The first one corresponds to carboxylic acid groups arising from the acid functionalization of the carbon material, which withstand the heat treatments carried out during catalyst preparation (Supplementary Informations S1). Temperature programmed desorption experiments performed on both the CNT support and the $Pd_{2\_SA/NP}$/CNT catalyst (Fig. S7) do not establish the presence of significant amounts of carboxylic groups after Pd deposition, these groups acting as anchoring sites for Pd.[50] DFT calculations performed on a Pd_{SA}/graphene single vacancy model show a charge transfer from Pd-*4d* to C-*2p* of -0.37 e- (Fig. S8). Thus, the second type of acidic sites consists in the Pd_{SA}, due to charge transfer from the metal to the support. The H_2-assisted isomerization of 1-octene (Fig. S9) was independently studied on various catalysts including: CNT support (with -COOH groups), $Pd_{2\_SA/NP}$/CNT, Pd/Al_2O_3 and a Pd_{SA}/CNT containing exclusively SA (Fig. 2d). CNT and the Pd_{SA}/CNT catalysts are almost inactive for 1-octene isomerization, and the $Pd_{2\_SA/NP}$/CNT clearly outperforms the Pd/Al_2O_3 catalyst. Thus, the presence of acidic sites that would assist the isomerization cannot explain the differences in reactivity observed. To gain further insight on the mechanistic pathway, DFT calculations were performed on Pd_{SA} and Pd_{NP} supported on graphene.

Mechanistic insights from DFT calculations

To study the isomerization and hydrogenation reactions, 2-butene was used as a model substrate (see Fig. 3). We considered first, the trapping of a Pd_{SA} in a mono-vacancy, which is strongly exothermic, with adsorption energy of roughly 100 kcal/mol. On Pd_{SA}, the hydrogenation and isomerization reactions begin with the exothermic (by 24.6 kcal/mol) π-coordination of 2-butene to Pd (**1**). From **1**, the isomerization (Fig. 3a) occurs *via* the formation of a π-allyl hydride intermediate as observed with homogeneous catalysts,[51] which requires to pass a high energy demanding transition state (36.4 kcal/mol) corresponding to the abstraction of one hydrogen atom from a methyl group. This leads to the formation of an unstable, by +34.4 kcal/mol with respect to **1** allyl intermediate (**2**). Then, the H atom is transferred with almost no barrier with respect to **2** (2.8 kcal/mol) to the carbon atom in alpha position of the methyl group, leading to the endothermic formation of but-1-ene (+4.8 kcal/mol with respect to **1**).

From **1**, the hydrogenation of the but-2-ene occurs through the Horiuti-Polanyi mechanism:[52] (*i*) alkene and H_2 coordination to Pd, (*ii*) H_2 dissociation, (*iii*) hydrogen transfer to one of the alkene methine carbon with formation of a σ-bond between Pd and the second C-methine, and finally (*iv*) reductive elimination of the free alkane. In our case (Figure 3b), the coordination of the 2-butene (**1**) and of a H_2 molecule (**4**) to the Pd_{SA} is exothermic. These initial steps are followed by an endothermic (+21.6 kcal/mol with respect to **4**) and kinetically demanding (activation barrier = +24.5 kcal/mol) H-H activation (**5**). This reaction exhibits a lower barrier than the isomerization reaction, by 9.9 kcal/mol. From **5**, the reaction continues by the transfer of one of the hydrogen atoms to one of the methine carbon atoms. The energy barrier of this last step is only +8.1 kcal/mol with respect to **5** but +29.7 kcal/mol with respect to **4**. This transfer induces the formation of a 2-butyl complex σ-coordinated to the Pd center (**6**), located at -11.7 kcal/mol with respect to the entrance channel. The subsequent reductive elimination occurs *via* an accessible transition state (+4.1 kcal/mol with respect to **6**) and leads to the exothermic formation of butane (-42.1 kcal/mol with respect to the separated reactants).

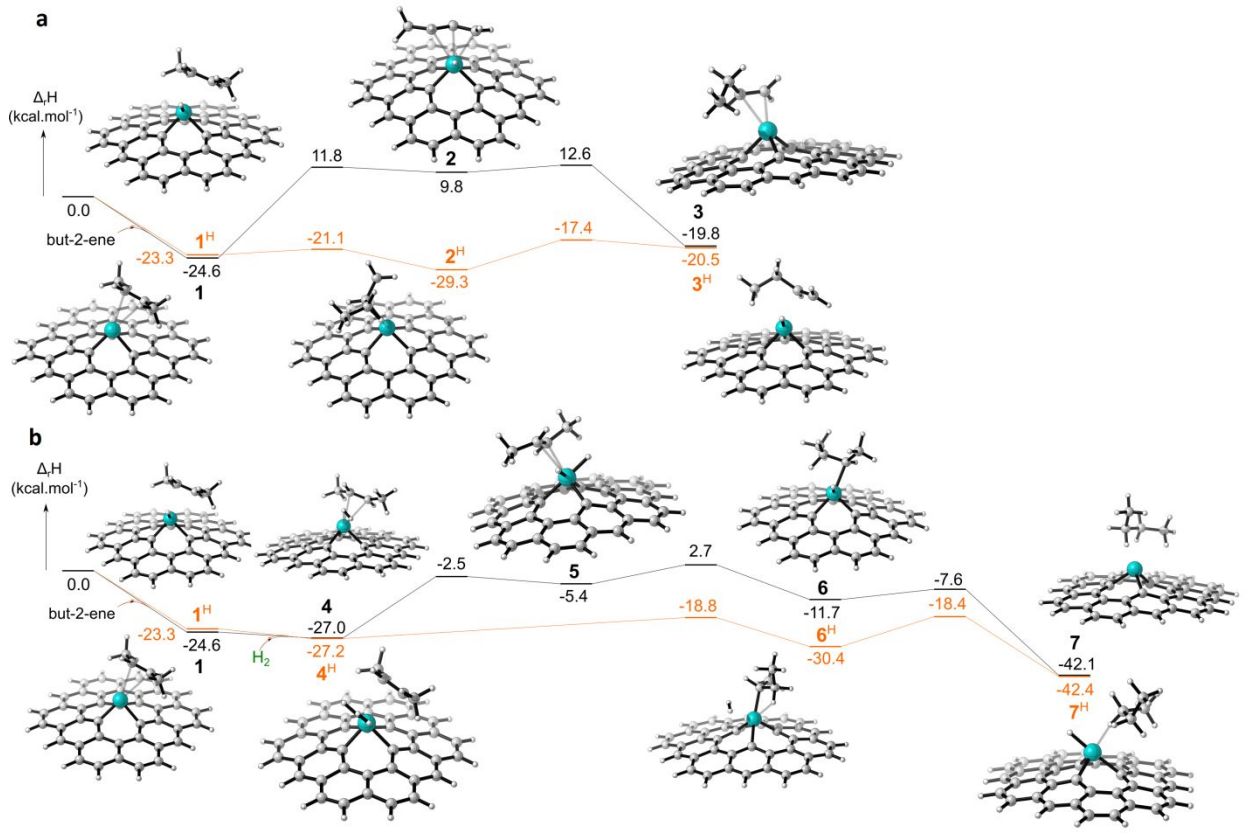

Figure 3. DFT mechanistic study. Reaction mechanisms of isomerization **a** and hydrogenation **b** of 2-butene mediated by Pd_{SA} and H-Pd_{SA} (in orange).

In summary, the hydrogenation of the 2-butene into butane is preferred both from a kinetic and thermodynamic point of view over the isomerization to 1-butene. However, according to the high barriers, a poor catalytic activity is expected in both cases, as experimentally observed for hydrogenation using single Pd atoms.[53,54] For comparison, an activation energy of 18 kcal/mol has been reported for the hydrogenation of 2-butene on a Pd_9/CNT catalyst.[55] In this context we also verified that the Pd_{SA}/CNT catalyst shows a very low activity for *β*-myrcene hydrogenation (see Fig. 7 in the section *Control of the single atoms/nanoparticles ratio*).

At this point, it is interesting to note that a completely different potential energy landscape is obtained if the catalyst is a hydrogenated SA (H-Pd_{SA}). A plausible scenario for the formation of this active site is: (i) a nearly barrierless activation of H_2 on Pd_{NP} (< 2kcal/mol on Pd_{13} supported on defective graphene monolayer), and (ii) hydrogen spillover. The latter has been widely studied in the context of hydrogen storage and catalysis, and many experimental studies report on that H-spillover can operate at low temperature on some carbon materials.[48,56-58] The entire spillover mechanism remains not fully understood; especially since some energy barriers remain high to be accessible at room temperature on non-defective carbon supports, but should correspond to a multi-step process after the dissociative adsorption of H_2 on Pd_{NP}. The H-migration from the NP to the carbon support is supposedly the first step with large energy barrier to overcome, and this step is not thermodynamically favorable for non-defective carbon supports. For instance a 60 kcal/mol energy barrier has been reported in the case of a Pt cluster on pristine graphene model, the final step being 35 kcal/mol above the initial one,[59] but when the graphene support is already hydrogenated the energy barrier is decreased and the thermodynamics become favorable.[60] However, it remains obscure how the support can be initially hydrogenated. Then H-diffusion on the carbon support occurs, with a relatively high energy barrier associated to a nearest-neighbor hopping process (> 20 kcal/mol on pristine carbon support).[44,58] Interestingly, it has also been proposed that the presence of oxygenated functional groups on the carbon support can facilitate the diffusion.[61] H-Clustering could also play a role by disturbing the sp^2 network around the H-adsorption site, decreasing significantly the energy barrier.[57,62] As we can see on Fig. 3b, the coordination of 2-butene to H-Pd_{SA} (**1^H**) remains exothermic, -23.3 kcal/mol with respect to the separated reactants. However, in this case the isomerization reaction takes place through a so-called metal hydride addition–elimination mechanism, strongly preferred for monohydrides. Thus, the isomerization proceeds *via* an initial hydrogen transfer to one of the –CH= carbons, followed by the dehydrogenation of the methyl group at α position with respect to the second methine carbon. This reaction is kinetically accessible with two low activation barriers (3.5 and 11.9 kcal/mol, respectively). However, even if the formation of the 2-butyl intermediate (**2^H**) is exothermic

with respect to $\mathbf{1^H}$ by -6.0 kcal/mol, that of the 1-butene product ($\mathbf{3^H}$) remains endothermic by +2.8 kcal/mol. Concerning the hydrogenation, the coordination of H_2 is followed by the transfer of the hydrogen atom to one of the methine carbons without H_2 dissociation. The corresponding activation barrier (8.4 kcal/mol above $\mathbf{4^H}$) corresponds to an easily kinetically accessible process. In the same way, the formation of the alkyl intermediate is found to be exergonic with respect to $\mathbf{4^H}$ (-3.2 kcal/mol with respect to $\mathbf{4^H}$). The last step corresponds to the heterolytic splitting of H_2 leading to the regeneration of the H-Pd_{SA} and the butane product ($\mathbf{7^H}$). The formation of butane is an exothermic process, by 25.2 kcal/mol with respect to $\mathbf{4^H}$ (-42.4 kcal/mol with respect to the separated reactant). The corresponding activation barrier for this step is 12 kcal/mol, compared to energy of 18 kcal/mol for a Pd_9 cluster supported on CNT[55] and 20 kcal/mol for a Pd/Al_2O_3 catalyst.[63] Therefore, this last step is the rate-determining step of an overall facile and exergonic reaction.

In order to confirm the key role of H-spillover in the cooperative catalysis between Pd_{SA} and Pd_{NP}, a $Pd_{2\_SA/NP}/CNT_{HT}$ catalyst (Fig. 2e) was prepared on CNT, from which the oxygen surface groups have been removed by thermal annealing at 1000 °C,[47] which should prevent H-spillover. Although this catalyst contains also a mixture of Pd_{SA} and Pd_{NP} (SA/NP = 2), with mean particle size similar to the $Pd_{2\_SA/NP}/CNT$ catalyst (Fig. S10) it shows a significantly reduced activity for myrcene hydrogenation (Fig. 4a), which is quite similar to the one of the Pd/Al_2O_3 catalyst that contains only Pd_{NP}. It is important to note here that such a behavior (*i.e.* a lower activity of Pd/C catalysts in the hydrogenation of myrcene on supports treated at 1000 ° C) has been systematically observed on various carbon supports and for catalysts exhibiting different particle sizes.[47] It is also worth mentioning that the two catalysts $Pd_{2\_SA/NP}/CNT$ and $Pd_{2\_SA/NP}/CNT_{HT}$ present a similar amount of Pd clusters (Pd_{NP} < 1 nm, Fig. S10), so that the observed high activity measured for the $Pd_{2\_SA/NP}/CNT$ catalyst cannot be only related to the presence of Pd clusters, even if it has been reported that noble metal clusters are often more active than nanoparticles.[64-67]

The hydrogen spillover was experimentally probed for these two CNT-supported catalysts. As it is well known that the spilled-over hydrogen migrates and readily reacts with the yellow WO_3 oxide to form dark blue H_xWO_3[68,69] we used the WO_3 tungsten oxide to diagnose the activation of H_2 on these two catalysts (Supplementary Informations S3). Such simple test was already used with success for Rh/zeolithe catalysts.[70] As shown in the photographs of Fig. 4b, the pure WO_3 did not change color after hydrogen treatment. When mixed with the $Pd_{2\_SA/NP}/CNT_{HT}$ catalyst, no significant change in color after the hydrogen treatment was observed. While this Pd catalyst should activate hydrogen, the absence of surface oxygen groups on the support does not allow extended hydrogen spillover. In contrast, when WO_3 was mixed with the $Pd_{2\_SA/NP}/CNT$ catalyst this resulted in the darkest color of the tungsten species after hydrogen treatment at 20 °C for 3 min, demonstrating that hydrogen dissociation and extended spillover occurred on this catalyst. We infer that the significant spillover should be attributed to the presence of oxygenated surface groups on the carbon support. These latter experiments confirm that the presence of oxygen surface groups is necessary for the cooperative catalysis to proceed *via* H-spillover.

The hydrogen spillover was also investigated by DFT, to propose a complete pathway, see Fig. 5, for the formation of H-Pd_{SA} species through the migration of H atoms initially adsorbed on H-saturated Pd_{NP}. As we can see on Fig. 5, the overall reaction is kinetically accessible and thermodynamically favorable. Our starting geometry is a H-saturated Pd_{NP} deposited on a defective di-vacancy with an oxygen atom in its vicinity. From this starting configuration the first H migration from the Pd_{NP} to the closest C atom in front of the ether group is thermodynamically favorable (-38 kcal/mol), with a reasonable energy cost (activation barrier = 10.2 kcal/mol). Then a second H can easily migrate (the energy barrier is less than 2 kcal/mol) to the same carbon atom leading to the formation of a $-CH_2$ group. Then we have evaluated the migration of one H from the $-CH_2$ group to a neighbor C carbon atom, still involved in the di-vacancy ring.

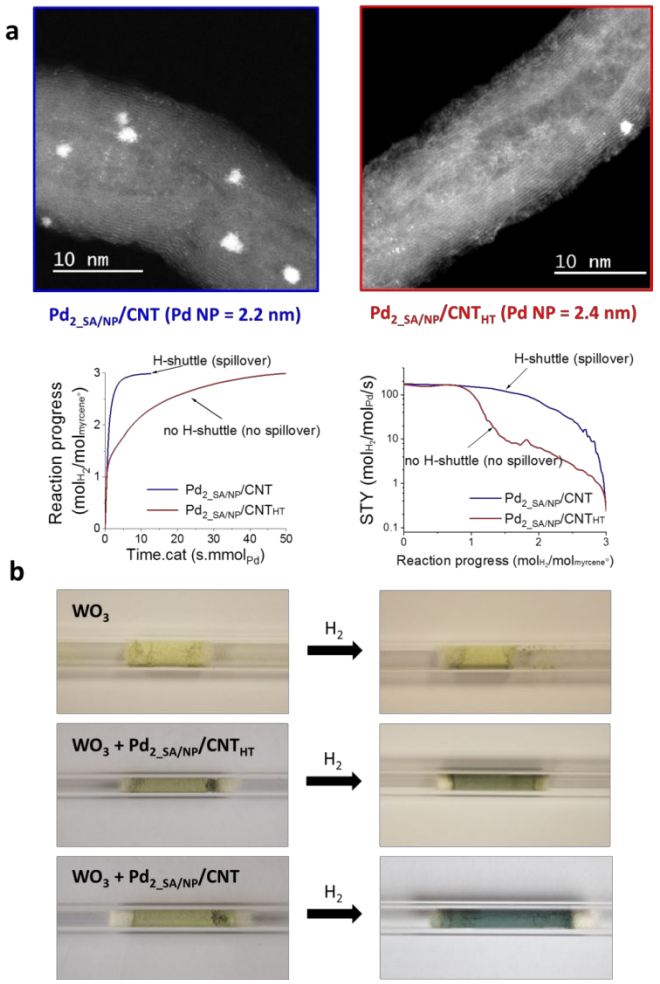

Figure 4. a β-Myrcene hydrogenation reactions carried out over $Pd_{2\_SA/NP}/CNT$ and $Pd_{2\_SA/NP}/CNT_{HT}$ catalysts. P_{H_2} = 20 bar - T = 120°C - β-myrcene 1 M (80 mL) – solvent heptane - 200 mg cat. **b** Photographs of samples made with 500 g of WO_3 mixed or not with 5 mg of catalyst before (left) and after (right) treatment with H_2 (100 mL/min) at 20 °C for 3 min.

This step, with an energy barrier of 29.7 kcal/mol, is the rate-determining step of the proposed profile. Then a second hopping process can proceed with a lower activation barrier (24.2 kcal/mol) to yield almost a single H atom adsorbed on the non-defective part of the carbon support. The adsorption of an extra H_2 molecule on Pd_{NP} ensures the overall stability of the H-migration process. Then H-diffusion can occur with an energy barrier of around 24 kcal/mol, in line with previous works, or can be significantly decreased to less than 9 kcal/mol, when the H atom is surrounded by other H atoms, 6 in the present case. Finally, the formation of the H-Pd_{SA} product takes places through a barrierless H transfer to Pd_{SA} with largely favorable stabilization energy of *ca.* -60.5 kcal/mol.

Thus, the correlation we have recently reported between the activity of Pd/C catalysts for β-myrcene hydrogenation and their structure,[47] which integrates the dispersion of the metal, and the quantity of oxygen groups and defects on the support, arises from a cooperative catalysis between Pd_{SA} and Pd_{NP} that involves H-spillover. It is certainly necessary to have highly dispersed Pd_{NP} on the support to activate H_2, but a high concentration of surface defects and oxygenated surface groups are also necessary on the carbon support, which favors the stabilization of Pd_{SA} and H-spillover, respectively. The resulting H-Pd_{SA} are highly active for alkene hydrogenation/isomerization.

Control of the single atoms/nanoparticles ratio

From the previous results, it becomes obvious that in heterogeneous catalysis, an ultra-rational use of precious metals often in short supply could pass by an accurate control of the SA/NP ratio. With this in mind, we have developed a simple process allowing the control of this ratio on carbon supports[20] to produce $Pd_{X\_SA/NP}$/CNT catalysts where X refers to the SA/NP ratio. Briefly, the process consists in: i) creating carboxylic groups on the support by nitric acid oxidation (step I); ii) decomposing these groups under an inert atmosphere to produce CO_2, carbon vacancies and some H_2 (step II); and iii) depositing the metal on this defective support (D-CNT, step III). On CNT support, the defective CNT produced after step II (D-CNT) contain defects that we have characterized by electron spin resonance (EPR) and vibrating sample magnetometry (VSM), and which can be used to stabilize metal single atoms. As for highly ordered pyrolytic graphite[72] the EPR spectrum of CNT presents a single peak, while that of D-CNT consists of two contributions (Fig. S11). The narrow line is associated to interacting conduction electrons, while the broad one corresponds to spin-polarized localized electronic states[73] As in the case of graphite, the magnetization curve of CNT presents a diamagnetic behavior, while for D-CNT ferromagnetism appears at room temperature, presumably due to the presence of defects (Fig. S12). Although the exact nature (vacancies or edges) of the localized electronic states created by the thermochemical process is not known, these defects efficiently stabilized Pd_{SA}. For a given metal loading, if step III is performed once, Pd_{SA} are selectively produced; and if it is performed several times, mixtures of SA and NP are obtained. The number of times that step III is performed for a given total metal loading, conditions the SA/NP ratio. Figure 6 shows TEM images of four 1.2% Pd/CNT samples prepared by this process, for which the SA/NP ratio is controlled between 200/1 (a single deposition cycle of 1.2% Pd) and 10/1 (four deposition cycles of 0.3% Pd).

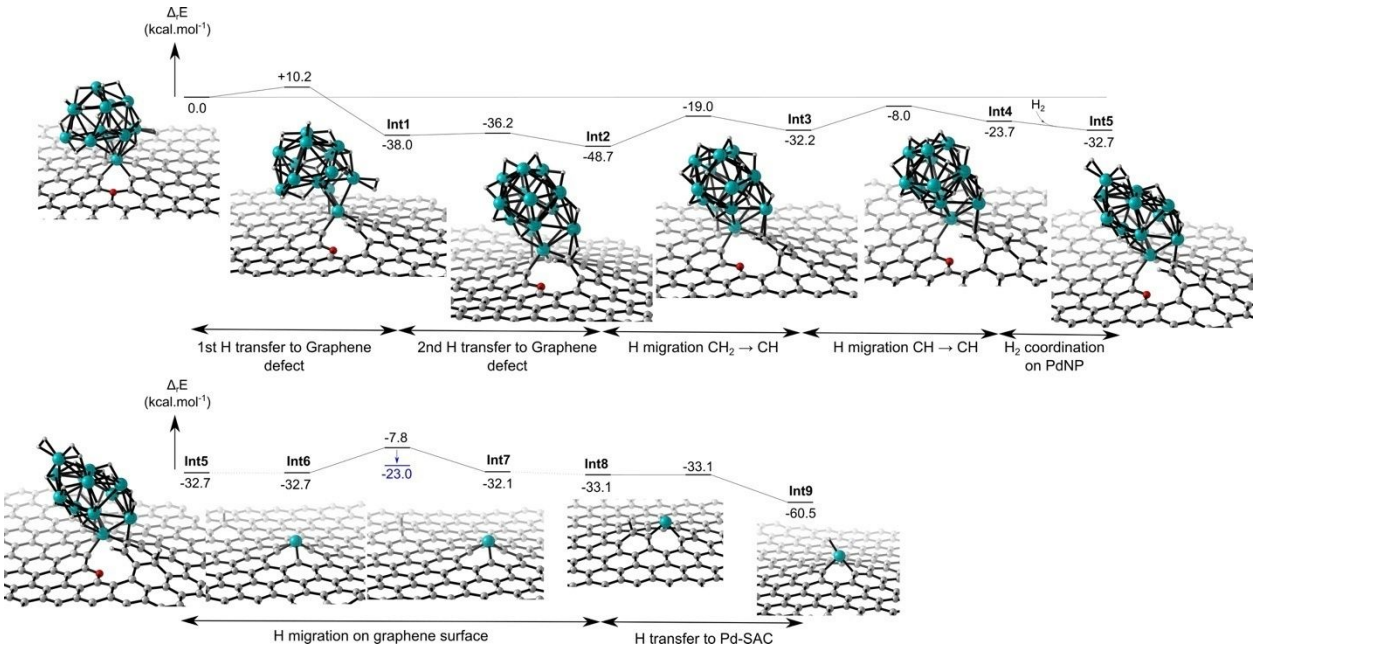

Figure 5. DFT mechanistic study. Spillover mechanism corresponding to the migration of H adsorbed on Pd_{NP} leading to the formation of H-Pd_{SA} species.

The particle size distribution based on total particle number and on total atom number are shown in Fig. S13.

As transmission electron microscopy only informs us thanks to a very local analysis of the samples (poor statistic value), we decide to use a more general probe to characterize the whole samples. Since traditional probe molecule infrared spectroscopy cannot been used for carbon supported catalyst, and EXAFS is not sensitive enough to identify SA in many cases,[74] we rely on XPS analyses. It is worth mentioning that the XPS analyses were performed on the four samples with introduction of the samples by vacuum transfer cell from a glove box under a controlled argon atmosphere, so we can exclude any air oxidation of this sample. The O 1*s* spectra exhibit large bands of the order of 5 eV, which suggests superposition of different oxygenated groups.[75] The line shapes are very similar for all samples and are close to the one of the D-CNT support (Fig. S14). Figure 7 shows the deconvolution of the Pd 3*d* spectra of the four samples. The binding energy at 335.3 eV is in agreement with the value reported in the literature for metallic palladium.[76] For the sample $Pd_{200\_SA/NP}$/CNT, this binding energy is slightly upshifted presumably due to charge transfer between the very small particles present on this sample and the support or to particle size-dependent shift.[77,78]

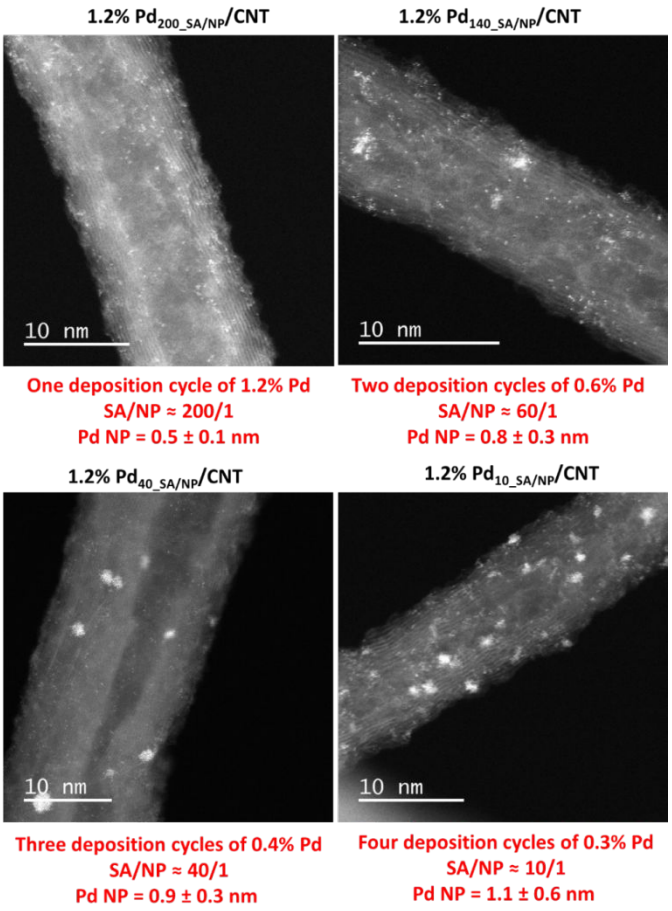

Figure 6. Mixtures of SA and NP at different ratio in 1.2% Pd/CNT catalysts.

The binding energy at 337.3 eV can be attributed to surface oxides and/or to electron-deficient palladium species ($Pd^{\delta+}$) such as SA or small clusters in strong interaction with the support.[79-81] The $Pd^{\delta+}/Pd^0$ ratio for the four samples are shown on Table 1 as well as the fraction of SA in the same samples determined from STEM. A good correlation was found between the results obtained with these two techniques (Fig. S15). These data, in association with the STEM-HAADF observations, confirm that the proportion of Pd_{SA} is much higher in the sample $Pd_{200\_SA/NP}$/CNT than in $Pd_{10\_SA/NP}$/CNT. Thus, this strategy allows engineering the minimal catalytic ensemble that will activate H_2 for the cooperative catalysis to operate.

For β-myrcene hydrogenation at 120 °C, regarding the catalysts tested, the optimum SA/NP ratio was found at 10/1 (Fig. 8). This optimal ratio offers the best control for the balance between H_2 activation on Pd_{NP}, the H-spillover and H-Pd_{SA} catalyzed β-myrcene hydrogenation rates. The activity of the $Pd_{10\_SA/NP}$/CNT (SA/NP = 10/1, Fig. 2f) outperformed the one of the $Pd_{2\_SA/NP}$/CNT catalyst (Fig. 8). At a reaction progress of 2, the STY with $Pd_{200\_SA/NP}$/CNT (SA/NP ≈ 200), $Pd_{2\_SA/NP}$/CNT (SA/NP ≈ 2), and $Pd_{10\_SA/NP}$/CNT (SA/NP ≈ 10) are 10, 44 and 272 s^{-1}, respectively (Fig. 8c). Once again, it is interesting to note that for this sample series, for which the surface chemistry of the support is the same, it is not the sample that presents a higher proportion of palladium clusters that is the more active.

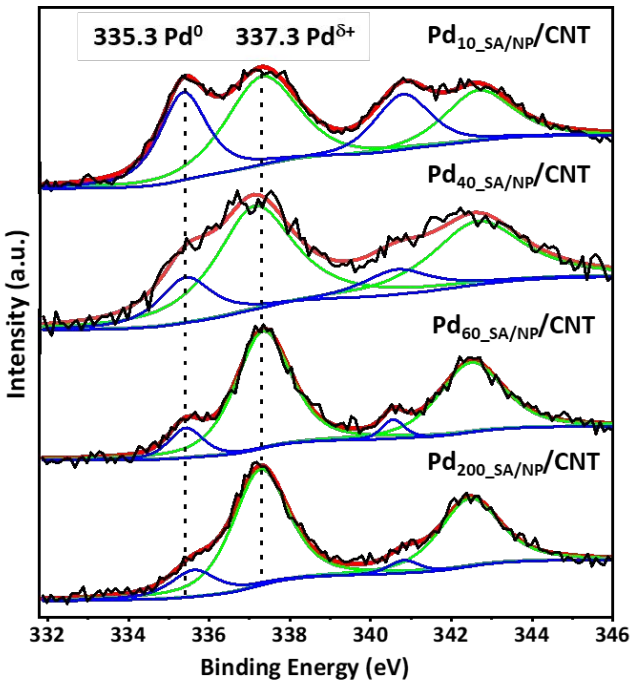

Figure 7. XPS spectra of Pd *3d* of $Pd_{200\_SA/NP}$/CNT, $Pd_{60\_SA/NP}$/CNT, $Pd_{40\_SA/NP}$/CNT and $Pd_{10\_SA/NP}$/CNT samples.

Table 1. Fraction of SA in the same samples determined from STEM and ratio $Pd^0/Pd^{\delta+}$ determined by XPS.

Sample	STEM fraction of SA (%)	XPS atomic percentage (%)		
		Pd^0	$Pd^{\delta+}$	$Pd^{\delta+}/Pd^0$
$Pd_{200\_SA/NP}$/CNT	0.97	14.21	85.79	6.06
$Pd_{60\_SA/NP}$/CNT	0.77	15.25	84.75	5.55
$Pd_{40\_SA/NP}$/CNT	0.61	22.00	78.00	3.55
$Pd_{10\_SA/NP}$/CNT	0.25	41.75	58.25	1.39

Thus, the sample $Pd_{60\_SA/NP}$/CNT present a similar proportion of Pd_{NP} < 1 nm based on total atoms than the sample $Pd_{10\_SA/NP}$/CNT (Fig. S13) but is significantly less active (Fig. 8c). Similarly, the sample $Pd_{200\_SA/NP}$/CNT, which presents a significant amount of clusters of different atomicity, is the less active of the series.

Finally, at a reaction progress of 2, there is a 44-fold increase of STY between the $Pd_{10\_SA/NP}$/CNT catalyst and $Pd_{2\_SA/NP}$/CNT_{HT} (a catalyst containing NP with no possibility of hydrogen spillover, see Fig. 4) and 195-fold increase with $Pd_{1000\_SA/NP}$/CNT (a catalyst containing almost exclusively SA). The evolution of STY with SA/NP ratio remains nearly the same for the reaction progress of 2.5 (Fig. 8c). This fact further confirms the consistency of these results.

Catalyst stability

Instead of running successive recyclability batch experiments catalyst stability was investigated through a dedicated continuous reactor operation. When a single typical batch experiment allows us to reach a moderate turn-over number (TON) of 6200 mol_{H2}/mol_{Pd}, the chosen continuous testing mode leads to TON values as high as 600 000 mol_{H2}/mol_{Pd}. This represents a more intensive and powerful way to test catalyst stability.[82] This contacting mode has also been chosen because of future developments within an intensified compact continuous reactor.

The continuous experiments were run with the $Pd_{2\_SA/NP}$/CNT catalyst coated on metallic open-cell solid foam cylinders. It is first worth mentioning that the coating process, performed at 300 °C under a nitrogen flow did not significantly modify the particle size distribution and the SA/NP ratio of the catalyst (Fig. S16a-f), pointing its good thermal stability. Such internals in milli-channels are ideal candidates to promote such powdered catalysts in a continuous reactor. The particularly confined hydrodynamics lead to interesting heat and mass transfer performances as well as a small pressure drop due to the wide-open structure of open-cell solid foams.[83-85] Fig. 9a presents the obtained evolution of the mean STY against the Turn Over Number (TON). As already mentioned, this mean STY cannot be compared to the instantaneous one followed in batch through H_2 consumption. Here it is calculated from a mass balance regarding outlet flow composition between myrcene, mono, di, and tri hydrogenated products. Depending on this distribution, the evolution of the corresponding reaction progress can be determined and is presented on Fig. 9b. First of all, it is noticeable that a very high TON of 600 000 mol_{H2}/mol_{Pd} is obtained, which is equivalent up to 100 recycling in batch mode with our typical conditions. Such a high TON is obtained because of the relatively low amount of Pd involved in the experiment (2 mg) together with a relatively long time on stream (>35 hours). Moreover, this indicates quite remarkable catalyst stability at all. The mean STY decreases quite regularly from 380 to 320 mol_{H2}/mol_{Pd}/min at the final TON value of 600 000 mol_{H2}/mol_{Pd}, which represent a loss of apparent activity of 15%.

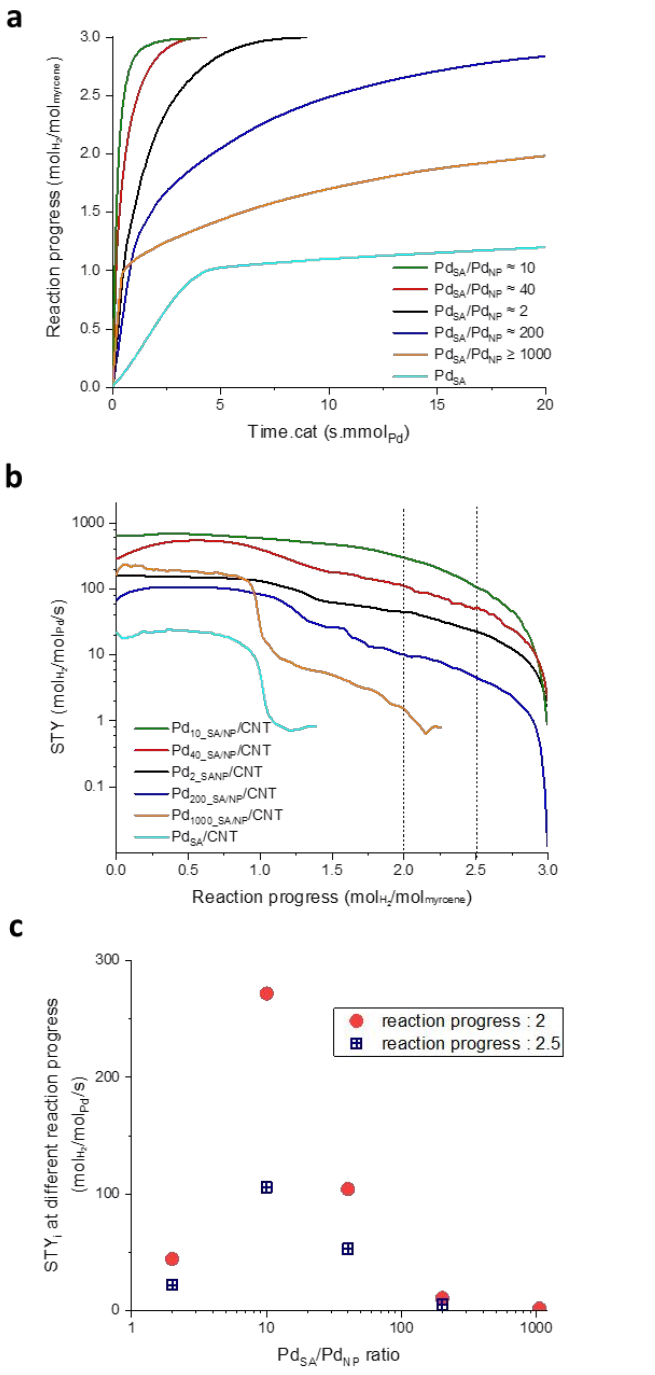

Figure 8. Catalytic results for myrcene hydrogenation at different SA/NP ratio. **a** Reaction progress as a function of time catalyst. **b** STY as a function of reaction progress. **c** STY at a reaction progress of 2 and 2.5 as a function of SA/NP ratio. Catalysts nomenclature is $Pd_{X\_SA/NP}$/CNT where X refers to the SA/NP ratio.

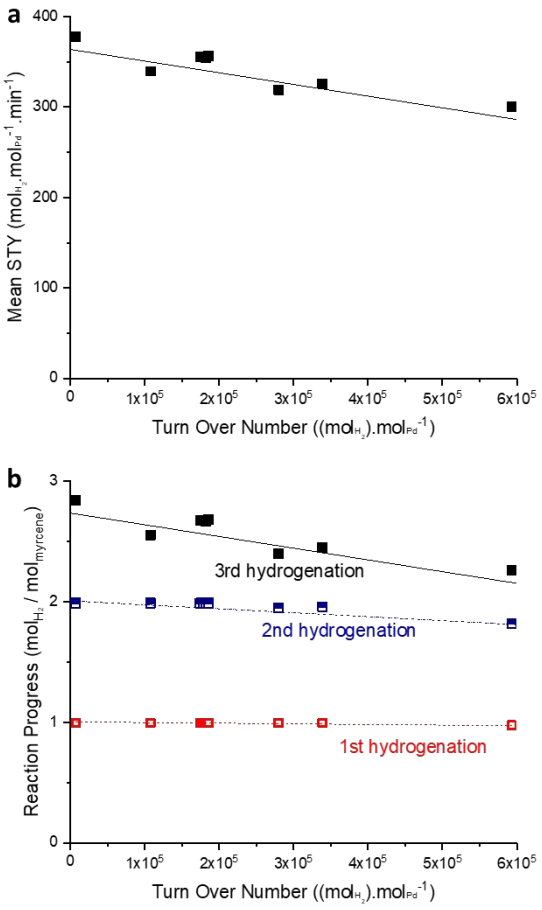

Figure 9. Catalyst stability testing in continuous mode using coated foam objects with $Pd_{2\_SA/NP}$/CNT catalyst (20 bar; 120 °C; 100 mg of catalyst; Q_L = 2 mL/min; Q_G = 2 NL/min, pure H_2; Myrcene 1M in heptane). **a**. Mean STY as a function of Turn Over Number. **b.** Reaction progress versus Turn Over Number.

The corresponding evolution of the outflow composition indicates that the reaction progress decreases also with decreasing contributions of the second and third hydrogenation while the first one remains constant. As in the batch experiments, this behavior for the first hydrogenation is explained by the gas-liquid external mass transfer limitation that hinder the intrinsic catalyst activity. For the slower second and third successive hydrogenations, the deactivation was logically more noticeable.

The coated catalyst was qualitatively examined by STEM-HAADF before and after this stability experiment (Fig. S16). After the test the SA/NP ratio changes from ≈ 2 to ≈ 3 and the mean Pd_{NP} size increased slightly from 2.5 to 3.2 nm. The slight deactivation could thus be structural but could also be explained by the strong adsorption of impurities from the natural starting material (β-myrcene). Although they could not be detected in the charge by GC because of their too low concentration, these impurities could continuously be absorbed on the catalyst, resulting in a gradual decrease in activity at high TON numbers. Studies are in due course to recover and characterize these adsorbed impurities.

Overall, the catalysts developed in this study appear resistant to sintering due to the stabilization of the SA by the functionalized carbon support and can undergo very long TON either in batch or continuous mode. Nonetheless in the chosen reaction, the catalysts appear sensible to a charge impurity and purification steps may be required to reach very high TON with a more stable activity over time. This fact was only detectable with the continuous mode operation because of its easier operability and ability to reach a very high TON. Moreover, in addition to efficient catalyst stability testing, the continuous mode operation appears very promising for the compact intensified and secure operation of this reaction.

Conclusion

Here, we have reported that a cooperative catalysis operates between carbon-supported Pd_{SA} and Pd_{NP} for alkene hydrogenation and isomerization, which involved: i) dihydrogen activation on Pd_{NP}, ii) H-spillover on the support, and iii) the catalytic reaction on H-P_{SA} species. This discovery provides a rational explanation for the structure/activity correlation that exists in Pd/C catalysts for myrcene hydrogenation,[47] which associates the metal dispersion (Pd_{NP} are necessary to activate H_2), the concentration of oxygen surface groups on the support (necessary for H-spillover), and the concentration of defects on the support (necessary for Pd^{SA} stabilization). While such a cooperative effect may occur in many Pd/C catalysts, it has never been recognized or exploited to improve catalytic performances in industrial catalysts. While this finding alone is important, major advances in heterogeneous catalysis can be achieved only if the SA/NP ratio can be controlled. Indeed, the control of this ratio, a major achievement of this work, allows tuning the catalyst performances. For β-myrcene hydrogenation, STY variations of several orders of magnitude were measured as a function of the value of this ratio. This work can also provide an explanation to the fact that many organic chemists experienced much contrasted catalytic performances for hydrogenation reactions with commercial Pd/C catalysts provided by different suppliers, since the Pd_{SA}/Pd_{NP} ratio is not controlled in such systems. Of course, other types of cooperative catalysis than the one reported herein can be envisioned, such as bifunctional catalysis with a single metal: metallic NP ensuring one function, and SA of the same element presenting an altered electronic density ensuring a second function. This has been recently proposed for the hydrogenation of aldehydes and ketones on Pd/TiO_2 catalysts.[7] Finally, our results demonstrate an interesting point for the single atom catalysis literature. Even when a very small number of metal NP are present (here Pd_{SA}/Pd_{NP} ratios of > 1000 or 200), the activity is quite different than the SA alone. This can be a common issue in studies that try to examine only the properties of SA but actually have a distribution of structures. Recent studies have started to point this out [15,86-89]

Conflicts of interest

The authors declare no competing financial interest.

Acknowledgements

We thank Vincent Collière (LCC, UPR8241 CNRS, Toulouse, France) for STEM analyses. B.F.M. acknowledges the exploratory project under the FCT Investigator Programme (ref. IF/00301/2015) with financial support from FCT/MCTES, through national funds (PIDDAC). C.R.C. thanks CONICYT for the financial support (Becas de doctorado en el extranjero "Becas Chile" - n° 72170200). R.C.C. thanks CONACYT for the financial support (PhD grant). I.C.G. and I.R. acknowledge the *Calcul en Midi-Pyrénées* initiative, CALMIP (Projects p0812 and p1214), for computer time allocation. This work was also granted access to the HPC resources of CINES and IDRIS under the allocation 2019-A0060906649 made by GENCI. Part of this work was performed within the framework of the ''DEEPER" project (in which LGPC members were involved) funded by the region Auvergne-Rhône-Alpes (contract number 15 021131 01 – CNR006) through the 20th FUI call. Part of this work was also supported by the Agence Nationale de la Recherche (ANR project ANR-19, COMET), which is gratefully acknowledged.

Notes and references

1. W. S. Lamme, O. van der Heijden, N. A. Krans, E. Nöllen, N. Mager, S. Hermans, J. Zečević and K. P. de Jong, *J. Catal*., 2019, **375**, 448-455.
2. U. Petek, F. Ruiz-Zepeda, M. Bele and Miran Gaberščček, *Catalysts*, 2019, **9**, 134.
3. A. Wang, J. Li and T. Zhang, *Nat. Rev. Chem*., 2018, **2**, 65-81.
4. G. Malta, S. A. Kondrat, S. J. Freakley, C. J. Davies, L. Lu, S. Dawson, A. Thetford, E. K. Gibson, D. J. Morgan, W. Jones, P. P. Wells, P. Johnston, C. R. A. Catlow, C. J. Kiely and G. J. Hutchings, *Science*, 2017, **355**, 1399-1403.
5. L. Liu and A. Corma, *Chem. Rev*., 2018, **118**, 4981-5079.
6. J. N. A. Tiwari, M. Harzandi, M. Ha, S. Sultan, C. W. Myung, H. J. Park, D. Y. Kim, P. Thangavel, A. Narayan, S. Pankaj, S. Selvaraj, S. Chandrasekaran, F. Salehnia, J.-W. Jang, H. S. Shin, Z. Lee and K. S. Kim, *Adv. Energy Mater*., 2019, **9**, 1900931.
7. L. Kuai, Z. Chen, S. Liu, E. Kan, N. Yu, Y. Ren, C. Fang, X. Li, Y. Li and B. Geng, *Nat. Commun*., 2020, **11**, 48.
8. Y. Ma, T. Yang, H. Zou, W. Zang, Z. Kou, L. Mao, Y. Feng, L. Shen, S. J. Pennycook, L. Duan, X. Li and J. Wang, *Adv. Mater*., 2020, **32**, 2002177.
9. J. Peng, Y. Chen, K. Wang, Z. Tang and S. Chen, *Int. J. Hydrog. Energy*, 2020, **45**, 18840-18849.
10. J. N. Tiwari, N. Kim Dang, H. Ju Park, S. Sultan, M. Gyu Kim, J. Haiyan, Z. Lee and K. S. Kim, *Nano Energy,* 2020, **78**, 105166.
11. R. Yun, F. Zhan, N. Li, B. Zhang, W. Ma, L. Hong, T. Sheng, L. Du, B.u Zheng and S. Liu, *Appl. Mater. Interfaces,* 2020, **12**, 34122−34129
12. A. O. King, R. D. Larsen and E.-i. Negishi, *in* Handbook of Organopalladium Chemistry for Organic Synthesis, E.-i. Negishi Ed., John Wiley & Sons, New York (2002) 2219-2752.
13. C. Rivera-Cárcamo and P. Serp, *ChemCatChem*, 2018, **10**, 5058-5091.
14. A. Granja-DelRío, J. A. Alonso and M. J. López, *J. Phys. Chem. C*, 2017, **121**, 10843-10850.
15. J. Resasco, F. Yang, T. Mou, B. Wang, P. Christopher and D. E. Resasco, *ACS Catal*., 2020, **10**, 595−603.
16. G. Kyriakou, M. B. Boucher, A. D. Jewell, E. A. Lewis, T. J. Lawton, A. E. Baber, H. L. Tierney, M. Flytzani-Stephanopoulos and E. C. H. Sykes, *Science*, 2012, **335**, 1209-1212.
17. L. Zhang, M. Zhou, A. Wang and T. Zhang, *Chem. Rev*., 2020, **120**, 683-733.
18. W. Liu, Y. Chen, H. Qi, L. Zhang, W. Yan, X. Liu, X. Yang, S. Miao, W. Wang, C. Liu, A. Wang, J. Li and T. Zhang, *Angew. Chem. Int. Ed.*, 2018, **57**, 7071-7075.
19. H. Yan, H. Lv, H. Yi, W. Liu, Y. Xia, X. Huang, W. Huang, S. Wei, X. Wu and J. Lu, *J. Catal*., 2018, **366**, 70-79.
20. P. Serp, C. Rivera-Cárcamo, R. Philippe and B. Guicheret, French patent FR1910044, 2019.
21. C.-T. Kuo, Y. Lu, L. Kovarik, M. Engelhard and A. M. Karim, *ACS Catal*., 2019, **9**, 11030-11041.
22. G. Kresse and J. Hafner, *Phys. Rev. B*, 1993, **47**, 558-561.
23. G. Kresse and J. Hafner, *Phys. Rev. B*, 1994, **49**, 14251-14269.
24. G. Kresse and J. Furthmüller, *Phys. Rev. B*, 1996, **54**, 11169-11186.
25. G. Kresse and J. Furthmüller, *Comput. Mater. Sci*., 1996, **6**, 15-50.
26. P. E. Blöchl, *Phys. Rev. B*, *1994*, **50**, 17953-17979.
27. G. Kresse and D. Joubert, *Phys. Rev. B*, 1999, **59**, 1758-1775.
28. J. P. Perdew, K. Burke and M. Ernzerhof, *Phys. Rev. Lett*., 1996, **77**, 3865-3868.
29. G. Henkelman, B. P. Uberuaga and H. Jónsson, *J. Chem. Phys.*, 2000, **113**, 9901-9904.
30. G. Henkelman and H. Jónsson, *J. Chem. Phys*., 2000, **113**, 9978-9985.
31. Gaussian09, revision D.01. M. J. Frisch, G. W. Trucks, H. B. Schlegel, G. E. Scuseria, , M. A. Robb, J. R. Cheeseman, G. Scalmani, V. Barone, B. Mennucci, G. A. Petersson, H. Nakatsuji, M. Caricato, X. Li, H. P. Hratchian, A. F. Izmaylov, J. Bloino, G. Zheng, J. L. Sonnenberg, M. Hada, M. Ehara, K. Toyota, R. Fukuda, J. Hasegawa, M. Ishida, T. Nakajima, Y. Honda, O. Kitao, H. Nakai, T. Vreven, J. A. Jr Montgomery, J. E. Peralta, F. Ogliaro, M. Bearpark, J. J. Heyd, E. Brothers, K. N. Kudin, V. N. Staroverov, T. Keith, R. Kobayashi, J. Normand, K. Raghavachari, A. Rendell, J. C. Burant, S. S. Iyengar, J. Tomasi, M. Cossi, N. Rega, J. M. Millam, M. Klene, J. E. Knox, J. B. Cross, V. Bakken, C. Adamo, J. Jaramillo, R. Gomperts, R. E. Stratmann, O. Yazyev, A. J. Austin, R. Cammi, C. Pomelli, J. W. Ochterski, R. L. Martin, K. Morokuma,V. G. Zakrzewski, G. A. Voth, P. Salvador, J. J. Dannenberg, S. Dapprich, A. D. Daniels, O. Farkas, J. B. Foresman, J. V. Ortiz, J. Cioslowski and D. J. Fox, Gaussian, Inc., Wallingford CT, 2013.
32. J. P. Perdew, J. A. Chevary, S. H. Vosko, K. A. Jackson, M. R. Pederson, D. J. Singh and C. Fiolhais, *Phys. Rev. B*, 1992, **46**, 6671-6687.
33. D. Becke, *J. Chem. Phys*., 1993, **98**, 5648-5652.
34. D. Andrae, 10.18419/opus-1359, 1989.
35. D. Andrae, U. Haeussermann, M. Dolg, H. Stoll and H. Preuss, *Theor. Chim. Acta*, 1990, **77**, 123-141.
36. A. W. Ehlers, M. Böhme, S. Dapprich, A. Gobbi, A. Höllwarth, V. Jonas, K. F. Köhler, R. Stegmann, A. Veldkamp and G. Frenking, *Chem. Phys. Lett*., 1993, **208**, 111-114.
37. R. Ditchfield, W. J. Hehre and J. A. Pople, *J. Chem. Phys*., 1971, **54**, 724-728.
38. W. J. Hehre, R. Ditchfield and J. A. Pople, *J. Chem. Phys*., 1972, **56**, 2257-2261.
39. P. C. Hariharan and J. A. Pople, *Theor. Chim. Acta*, 1973, **28**, 213 – 228.
40. P. C. Hariharan and J. A. Pople, *Mol. Phys*., 1974, **27**, 209-214.
41. M. M. Franci, W. J. Pietro, W. J. Hehre, J. S. Binkley, M. S. Gordon, D. J. DeFrees and A. J. Pople, *J. Chem. Phys*., 1982, **77**, 3654-3665.
42. T. Clark, J. Chandrasekhar, G. W. Spitznagel and P. V. R. Schleyer, *J. Comput. Chem*., 1983, **4**, 294-301.

43. M. J. Frisch, J. A. Pople and J. S. Binkley, *J. Chem. Phys*., 1984, **80**, 3265-3269.
44. S. Grimme, S. Ehrlich and L. Goerigk, *J. Comput. Chem*., 2011, **32**, 1456-1465.
45. P. Baeckström, L. Li, M. Wickramaratne and T. Norin, *Synth. Commun*., 1990, **20**, 423-429.
46. F. Simescu Lazar, T. Chaieb, S. Pallier, L. Veyre, R. Philippe and V. Meille, *Appl. Catal. A: General,* 2015, **508**, 45-51.
47. R. Castro Contreras, B. Guicheret, B. F. Machado, C. Rivera-Cárcamo, M. A. Curiel Alvarez, B. Valdez Salas, M. Ruttert, T. Placke, A. Favre Réguillon, L. Vanoye, C. de Bellefon, R. Philippe and P. Serp, *J. Catal*., 2019, **372**, 226-244.
48. I. C. Gerber and P. Serp, *Chem. Rev*., 2020, **120**, 1250-1349.
49. E. Bogel-Łukasik, M. Gomes da Silva, I. D. Nogueira, R. Bogel-Łukasik and M. Nunes da Ponte, *Green Chem*., 2009, **11**, 1847-1856.
50. B. F. Machado, M. Oubenali, M. Rosa Axet, T.Trang Nguyen, M. Tunckol, M. Girleanu, O. Ersen, I. C. Gerber and P. Serp, *J. Catal*., 2014, **309**, 185-198.
51. G. A. Olah and Á. Molnár, Hydrocarbon chemistry, (John Wiley & Sons, Inc. 2003).
52. I. Horiuti and M. Polanyi, *Trans. of Faraday Soc.*, 1934, **30**, 1164-1172.
53. H. Gentsch, N. Guillen and M. Köpp, *Z. Phys. Chem*., 1972, **82**, 49-57.
54. M. D. Rossell, F. J. Caparrós, I. Angurell, G. Muller, J. Llorca, M. Secob and O. Rossell, *Catal. Sci. Technol*., 2016, **6**, 4081-4085.
55. V. D'Anna, D. Duca, F. Ferrante and G. La Manna, *Phys. Chem. Chem. Phys*., 2010, **12**, 1323-1330.
56. Y. Lin, F. Ding, B. I. Yakobson, Phys. Rev. B 78 (2008) 759-764.
57. V. A. Borodin, T. T. Vehvilainen, M. G. Ganchenkova and R. M. Nieminen, *Phys. Rev. B*, 2011, **84**, 075486(15).
58. D. S. Pyle, E. M. Gray and C. J. Webb, *Int. J. Hydrog. Energy*, 2016, **41**, 19098-19113.
59. G. M. Psofogiannakis and G. E. Froudakis, *J. Phys. Chem. C*, 2009, **113**, 14908-14915.
60. A. K. Singh, M. A. Ribas and B. I. Yakobson, *ACS Nano*, 2009, **3**, 1657-1662.
61. G. M. Psofogiannakis and G. E. Froudakis, *J. Am. Chem. Soc*., 2009, **131**, 15133-15135.
62. Y. Ferro, F. Marinelli and A. Allouche, *Chem. Phys. Lett*., 2003, **368**, 609-615.
63. G. C. Bond and J. M. Winterbottom, *Trans. Faraday Soc*., 1969, **65**, 2779-2793.
64. A. A. Herzing, C. J. Kiely, A. F. Carley, P. Landon and G. J. Hutchings, *Science*, 2008, **321**, 1331-1335.
65. Y. Lei, F. Mehmood, S. Lee, J. Greeley, B. Lee, S. Seifert, R. E. Winans, J. W. Elam, R. J. Meyer, P. C. Redfern, D. Teschner, R. Schlögl, M. J. Pellin, L. A. Curtiss and S. Vajda, *Science*, 2010, **328**, 224-228.
66. A. Corma, P. Concepción, M. Boronat, M. J. Sabater, J. Navas, M. J. Yacaman, E. Larios, A. Posadas, M. A. López-Quintela, D. Buceta, E. Mendoza, G. Guilera and A. Mayoral, *Nat. Chem*., 2013, **5**, 775-781.
67. T. Imaoka, Y. Akanuma, N. Haruta, S. Tsuchiya, K. Ishihara, T. Okayasu, W.-J. Chun, M. Takahashi and K. Yamamoto, *Nat. Commun*. 2017, **8**, 688.
68. S. Khoobiar, *J. Phys. Chem*., 1964, **68**, 411-412.
69. Y. Xi, Q. Zhang and H. Cheng, *J. Phys. Chem. C*, 2014, **118**, 494-501.
70. C. Wang, E. Guan, L. Wang, X. Chu, Z. Wu, J. Zhang, Z. Yang, Y. Jiang, L. Zhang, X. Meng, B. C. Gates and F.-S. Xiao, *J. Am. Chem. Soc*., 2019, **141**, 8482-8488.
71. M. Blanco-Rey, J. I. Juaristi, M. Alducin, M. J. López and J. A. Alonso, *J. Phys. Chem. C*, 2016, **120**, 17357-17364.
72. S. Łoś, L. Duclaux, W. Kempiński and M. Połomska, *Micropor. Mesopor. Mat*., 2010, **130**, 21-25.
73. L. Ćirić, A. Sienkiewicz, D. M. Djokić, R. Smajda, A. Magrez, T. Kaspar, R. Nesper and L. Forró, *Phys. Status Solidi B*, 2010, **247**, 2958-2961.
74. K. Feng, H. Zhang, J. Gao, J. Xu, Y. Dong, Z. Kang and J. Zhong, *Appl. Phys. Lett*. 2020, **116**, 191903.
75. A. B. Dongil, B. Bachiller-Baeza, A. Guerrero-Ruiz, I. Rodríguez-Ramos and A. Martínez-Alonso, *J. Colloid Interface Sci*., 2011, **355**, 179-189.
76. A. L. Dantas Ramos, P. da Silva Alves, D. A. G. Aranda and M. Schmal, *Appl. Catal. A: General*, 2004, **277**, 71-81.
77. A. Fritsch and P. Légaré, *Surf. Sci*., 1985, **162**, 742-746.
78. I. Aruna, B. R. Mehta, L. K. Malhotra and S. M. Shivaprasad, *J. Appl. Phys*., 2008, **104**, 064308.
79. R. G. Rao, R. Blume, T. W. Hansen, E. Fuentes, K. Dreyer, S. Moldovan, O. Ersen, D. D. Hibbitts, Y. J. Chabal, R. Schlögl and J.-P. Tessonnier, *Nat. Commun*., 2017, **8**, 340.
80. W. Xiang, Y. Zhao, Z. Jiang, X. Li, H. Zhang, Y. Sun, Z. Ning, F. Du, P. Gao, J.g Qian, K. Kato, M. Yamauchi and Y. Sun, *J. Mater. Chem. A*, 2018, **6**, 23366-23377.
81. J. Xi, H. Sun, D. Wang, Z. Zhang, X. Duan, J. Xiao, F. Xiao, L. Liu and S. Wang, *Appl. Catal. B: Environmental*, 2018, **225**, 291-297.
82. S. L. Scott, *ACS Catal*., 2018, **8**, 8597-8599.
83. J.-N. Tourvieille, R. Philippe and C. de Bellefon, *Chem. Eng. J*., 2015, **267**, 332-346.
84. M. Serres, D. Schweich, V. Vidal and R. Philippe, *Chem. Eng. Sci*., 2018, **190**, 149-163.
85. A. Avril, C. H. Hornung, A. Urban, D. Fraser, M. Horne, J.-P. Veder, J. Tsanaktsidis, T. Rodopoulos, C. Henry and D. R. Gunasegaram, *React. Chem. Eng*., 2017, **2**, 180-188.
86. C.-T. Kuo, Y. Lu, L. Kovarik, M. Engelhard and Ayman M. Karim, *ACS Catal*., 2019, **9**, 11030-11041.
87. L. Liu, D. M. Meira, R. Arenal, P. Concepcion, A. V. Puga, and Avelino Corma, *ACS Catal*., 2019, **9**, 10626-10639.
88. J. Resasco, L. DeRita, S. Dai, J. P. Chada, M. Xu, X. Yan, J. Finzel, S. Hanukovich, A. S. Hoffman, G.e W. Graham, S. R. Bare, X.g Pan and P. Christopher, *J. Am. Chem. Soc.,* 2020, **142**, 169-184.
89. S. Mitchell and J. Pérez-Ramírez, *Nat. Commun*., 2020, **11**, 4302.

Graphical abstract

Herein, we show that the control of the single atom/nanoparticle ratio in Pd/C allows the development of a new generation of highly active hydrogenation catalysts integrating the ultra-rational use of Pd.

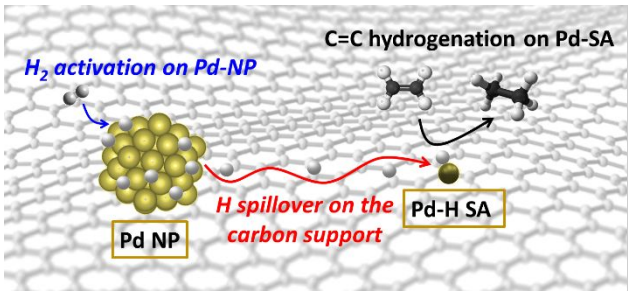

Electronic Supplementary Information

Control of the single atoms/nanoparticles ratio in Pd/C catalysts to optimize the cooperative hydrogenation of alkenes

Authors: C. Rivera-Cárcamo, I. C. Gerber, I. del Rosal, B. Guicheret, R. Castro Contreras, L. Vanoye, A. Favre-Réguillon, C. de Bellefon, R. Philippe, P. Serp

This file includes:

Materials and Methods

S.1 Materials

Carbon nanotube synthesis. A homemade $AlFeCoO_4$ catalyst was reduced in a fluidized bed reactor under a nitrogen (225 $mL \cdot min^{-1}$) and hydrogen (150 $mL \cdot min^{-1}$) flow at 650 °C. After the reduction step, the ethylene flow was adjusted to 225 $mL \cdot min^{-1}$ for 30 min to produce CNT. The CNT were recovered and then purified using an aqueous solution (50 vol% H_2SO_4) under reflux at 140 °C for 3 h. The acidic solution was then filtered and the solid washed with distilled water. The resulting solid was dried in an oven at 80 °C overnight. A portion of purified CNT was then functionalized with HNO_3 under reflux at 140 °C for 3 h. The acidic solution was filtered and washed with distilled water. The resulting solid was dried in an oven at 80 °C overnight to produce functionalized CNT (CNT). Another portion of purified CNT was treated in a horizontal tube oven under a nitrogen flow at 1000 °C for 1 h to produce high-temperature-treated CNT_{HT}. Finally, for EPR and VSM analyses, a portion of CNT (CNT_{ox}) was treated at 2800 °C for 1 h to produce high-temperature-treated CNT free of metallic impurities.

Palladium catalyst synthesis.

Supplementary Table 1. Catalysts properties.

Catalyst	Pd loading (%)	NP size from TEM (nm)[a)]	Pd dispersion (%)[c)]	SA/NP ratio[d)]
Pd/Al_2O_3	5	3.9 ± 1.1	31	n.d.[e)]
Pd/C	5	2.4 ± 1.0	46	n.d.[e)]
Pd/CNT also named **$Pd_{2\_SA/NP}/CNT$**	2	2.2 ± 1.1	49	2
$Pd_{2\_SA/NP}/CNT_{HT}$	1.6	2.2 ± 1.1	49	2
Pd_{SA}/CNT	0.1	-	-	no NP
$Pd_{1000\_SA/NP}/CNT$	0.1	1 ± 0.5[b)]	-	1000
$Pd_{200\_SA/NP}/CNT$	1.2	0.5 ± 0.1	-	200
$Pd_{60\_SA/NP}/CNT$	1.2	0.8 ± 0.3	-	60
$Pd_{40\_SA/NP}/CNT$	1.2	0.9 ± 0.3	-	40
$Pd_{10\_SA/NP}/CNT$	1.2	1.1 ± 0.6	-	10
Pd/FLG	1.9	2.6 ± 1.6	43	10
Pd/CNF	1.7	1.5 ± 0.9	67	n.d.[e)]

a) Calculated over 300 NP from STEM-HAADF micrographs
b) Calculated over 20 NP from STEM-HAADF micrographs
c) Metal dispersion was evaluated from a universal mathematical relation between the mean relative size of metallic crystallites and their dispersion [1].
d) SA/NP ratio in number calculated over 500 elements from STEM-HAADF micrographs.
e) n.d.: not determined

S.2 Catalytic experiments

H_2-assisted isomerization of 1-octene

Isomerization of alkenes was assessed using a dedicated experience. 1-octene was used as a molecular probe (see scheme below). The different isomers and by-product that could be obtained during the isomerization of 1-octene by Pd catalysts is shown below:

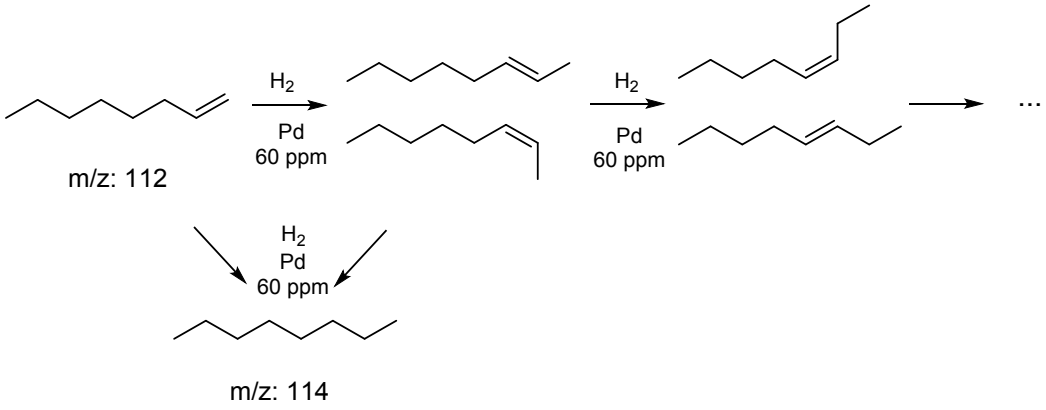

H_2-assisted isomerization of 1-octene

60 mL of a solution of 1-octene (Sigma Aldrich, 99%) in heptane (1 M) was added in a 100 mL round bottom flask and then heat at reflux under H_2 atmosphere. A sample was taken for *ex-situ* analysis and then catalyst was added in one portion. The mass of the catalyst was adjusted in order to have 3.75 µmol of Pd (0.4 mg, 60 ppm). Samples were taken as the function of time and were analyzed using GC-FID analysis.

The concentration of isomers of 1-octene and octane could be easily followed by GC as shown below.

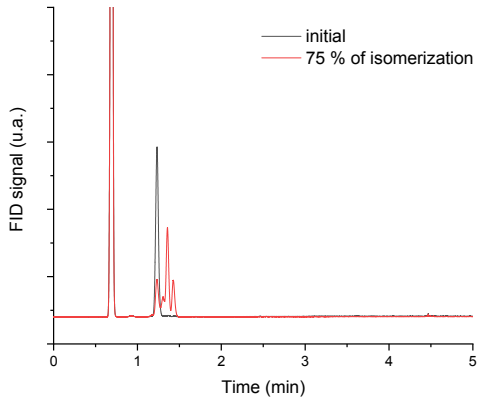

GC-FID of the reaction mixture

The absence of hydrogenation product (*i.e. n*-octane) was assessed by comparison with pure octane and by GC-MS analysis (see chromatogram below). Under those conditions, no hydrogenation product (*i.e.* n-octane) could be identified in the reaction mixture. This was

confirmed by comparison with pure octane and by GC-MS analysis in SIM mode (see chromatogram below).

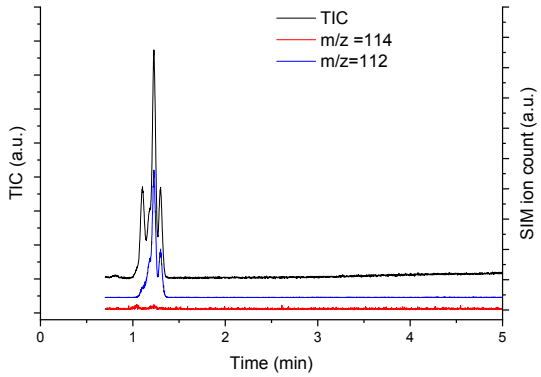

GC-MS chromatogram TIC and SIM ion count of a sample at 75 % of isomerization. Reaction conditions: 1 M 1-octene in heptane (1 M), reflux (98°C), H_2 1 atm.

The comparison of the 1-octene isomerization by the Pd catalysts is shown inFig. S.

S.3. Tests to assess hydrogen spillover

To check for the H-spillover, we used WO_3 to diagnose the activation of H_2 in the various catalysts, because the spilled-over hydrogen migrates and readily reacts with the yellow WO_3 to form dark blue H_xWO_3 [2]. Samples made with 500 g of WO_3 were mixed or not with 5 mg of catalyst and treated with H_2 (100 mL/min) at 20 °C for 3 min.

S.4 Assessment of the impact of mass transfer for myrcene hydrogenation

Mass transfer limitations have been evaluated using common chemical engineering approaches regarding the limiting reagent H_2. The physical properties of the different phases involved in the reaction are listed in the following Supplementary Table 2. Gas and liquid properties are given for 20 bar and 120 °C.

Supplementary Table 2: Physical properties of the different phases at 120 °C and 20 bar.

Phase	Name	Symbol	Value	Units
Liquid	Viscosity[a]	μ_L	1.71×10^{-4}	Pa.s
	Density	ρ_L	703	kg/m^3
	Surface tension[a]	σ_L	1×10^{-2}	N/m
	H_2 diffusivity[a]	$D_{m,H2}$	1.99×10^{-9}	m^2/s
	H_2 solubility[b]	C^*_{H2}	187	mol/m^3_L
Gas	Viscosity[a]	μ_G	1.07×10^{-5}	Pa.s
	Density	ρ_G	1.22	kg/m^3
CNT support	Skeleton density[c]	ρ_S	1900	kg/m$^3_{skeleton}$
	Pore volume[d]	V_{pore}	2.5	mL/g
	Dry particle density[d]	ρ_P	600	kg/m$^3_{particle}$
	Wetted particle density	ρ_p	1080	kg/m$^3_{particle}$
	Internal porosity[e]	β_P	70%	m$^3_{void}$/m$^3_{particle}$
	Tortuosity[f]	τ	≈1	-
	Mean Particle (agglomerate) diameter[4]	d_P	1-2	µm
γ-Al_2O_3 support	Skeleton density	ρ_S	3650	kg/m$^3_{skeleton}$
	Dry particle density	ρ_P	1460	kg/m$^3_{particle}$
	Wetted particle density	ρ_p	1880	kg/m$^3_{particle}$
	Internal porosity	β_P	60%	m$^3_{void}$/m$^3_{particle}$
	Tortuosity	τ	≈ 3	-
	Mean Particle diameter	d_P	25	µm
Activated Carbon support	Skeleton density[c]	ρ_S	1900	kg/m$^3_{skeleton}$
	Dry particle density	ρ_P	760	kg/m$^3_{particle}$
	Wetted particle density	ρ_p	1180	kg/m$^3_{particle}$
	Internal porosity	β_P	60%	m$^3_{void}$/m$^3_{particle}$
	Tortuosity	τ	≈ 3	-
	Mean Particle diameter	d_P	10	µm

a) Estimated using correlations found in [3].
b) Thermodynamic calculations with PPR78 group contribution using PROSIM software for a flash equilibrium at constant P & T.
c) Commonly taken equal to the graphite density.
d) See for example [4,5] for such typical orders of magnitudes.
e) Calculated from skeleton density and pore volume.
f) See [6] for a discussion about mass transfer inside nanotubes bundles.

S.4.1. G-L external mass transfer

To evaluate the efficiency of the reactor set up to transfer hydrogen in the liquid phase, the mass transfer coefficient (k_La_{GL}) of the reactor has been measured experimentally with a classical physical absorption technique [7, 8] following the H_2 consumption in the regulated and calibrated gas tank. Identical conditions to the experimental ones have been used but without any catalyst (1200 rpm, 80mL of 1M myrcene solution in heptane, 120°C, constant P_{H2} = 20 bar). The H_2 consumption profile of the reserve allowed adjusting and recovering 2 parameters of the system mass balance (eq. S1-S3): the mass transfer coefficient k_La_{GL} and the final saturation concentration of H_2 in the solution (solubility) C^*_{H2}.

$$dn^L_{H2}(t) = -\,dn^{Res}_{H2}(t) = -dp^{res}(t)\frac{V_{res}}{RT_{res}} \quad \text{(S1)}$$

$$\boldsymbol{k_La_{GL}}V_R\left(\boldsymbol{C^*_{H2}} - C^L_{H2}(t)\right) = \frac{dn^L_{H2}(t)}{dt} = V_L\frac{dC^L_{H2}(t)}{dt} \quad \text{(S2)}$$

$$-dp^{res}(t) = \frac{RT_{res}}{V_{res}}\boldsymbol{C^*_{H2}}V_L\left(1 - exp\left(-\frac{\boldsymbol{k_La_{GL}}}{\varepsilon_L}t\right)\right) \quad \text{(S3)}$$

In these equations, $dn^L_{H2}(t)$ is the variation of the quantity of dissolved H_2 in the liquid phase between t_0 and t (mol); $dn^{Res}_{H2}(t)$ is the corresponding variation of H_2 in the calibrated reserve (mol); $dp^{res}(t)$ is the corresponding pressure variation in the reserve (Pa); V_{res} is the volume of

the reserve (m^3) ; T_{res} is the temperature of the reserve (K) ; V_L is the liquid volume inside the reactor (m^3) ; ε_L is the liquid fraction inside the reactor (m^3_L/m^3_R) ; C^*_{H2} is the solubility of H_2 in the liquid mixture (mol/m^3); $k_L a_{GL}$ is the G-L mass transfer coefficient (s^{-1}) with $a_{GL}$the specific surface area for G-L mass transfer ($m^2_{GL}/m^3_{Reactor}$).

$k_L a_{GL}$ and C^*_{H2}were estimated as 0.2 s^{-1} and 190 mol_{H2}/m^3_L respectively. The $k_L a_{GL}$ appears typical of well-equipped laboratory stirred tank reactor (for H_2). The experimental solubility is in agreement with the one calculated with the PPR78 thermodynamic model (187 mol/m^3_L).

Based on these mass transfer measurements, a theoretical maximum H_2 consumption, $F^{max,GL}_{H2}$ (in mol_{H2}/s) can be defined for each experiment (S4). This consumption can be linked to the corresponding theoretical apparent reaction rate, $\overline{r^{max}_{p,app}}$ (S5), or to the corresponding theoretical Site Time Yield, STY^{max} (S6), both in full G-L mass transfer regime:

$$F^{max,GL}_{H2} = k_L a_{GL} V_R C^*_{H2} \quad \text{(S4)}$$

$$\overline{r^{max,GL}_{p,app}} = \frac{F^{max,GL}_{H2}}{V_{cata}} = \frac{k_L a_{GL} V_R C^*_{H2}}{V_{cata}} \quad \text{(S5)}$$

$$STY^{max,GL} = \frac{F^{max,GL}_{H2}}{n_{Pd}} = \frac{k_L a_{GL} V_R C^*_{H2}}{n_{Pd}} \quad \text{(S6)}$$

Independently, following the instantaneous consumption curves of H_2, experimental instantaneous apparent reaction rates or STY can be determined at any reaction progress. These latter can be compared to the corresponding theoretical ones to appreciate a fraction of external G-L mass transfer limitation, f^{GL}_{ex} (S7), on the measurements and is analogous of the L-S external mass transfer one because no reaction occurs inside the liquid, only on the catalyst surfaces.

$$f^{GL}_{ex} = \frac{STY}{STY^{max,GL}} = \frac{\overline{r_{p,app}}}{\overline{r^{max}_{p,app}}} \quad \text{(S7)}$$

The relationship between the instantaneous STY and the instantaneous apparent reaction rate $\overline{r_P}$, (per volume of wetted catalyst) is recalled in (S8) :

$$\overline{r_P} = \frac{STY \times \rho_P \times wt.\%_{Pd}}{M_{Pd}} \quad \text{(S8)}$$

Supplementary Table 3 presents this determination for most of the catalysts of the study (those of Figures 1 and 7) at three different reaction progresses: 0.5 $mol_{H2}/mol_{myrcene}$, 2.0 $mol_{H2}/mol_{myrcene}$ and 2.5 $mol_{H2}/mol_{myrcene}$.

Supplementary Table 3: Appraisal of G-L mass transfer limitations.

Catalyst	n_{Pd} (µmol)	STY^{max} ($mol_{H2}/s/mol_{Pd}$)	$STY_{0.5}$ ($mol_{H2}/s/mol_{Pd}$)	$f_{ex,0.5}^{GL}$ (-)	E (-)	$STY_{2.0}$ ($mol_{H2}/s/mol_{Pd}$)	$f_{ex,2.0}^{GL}$ (-)	$STY_{2.5}$ ($mol_{H2}/s/mol_{Pd}$)	$f_{ex,2.5}^{GL}$ (-)
Pd/Al_2O_3	37.6	199	109	55%	1.0	10.2	5%	4.6	2%
Pd/C	36.5	205	168	82%	1.0	72	35%	26	13%
Pd/CNT **also named** $Pd_{2\_SA/NP}/CNT$	38.3	195	144	74%	1.0	44	23%	22	11%
$Pd_{1000\_SA/NP}/CNT$	1.9	3979	184	5%	1.0	1.4	0.04%	N.A.	N.A.
$Pd_{200\_SA/NP}/CNT$	25.0	299	104	35%	1.0	10.4	3%	4.5	2%
$Pd_{40\_SA/NP}/CNT$	25.8	290	544	**187%**	**1.9**	104	19%	50	9%
$Pd_{10\_SA/NP}/CNT$	24.2	308	672	**218%**	**2.2**	272	40%	106	16%

First of all, it is noticeable that the STY^{max} reached different values depending on the different amounts of Pd in each experiment. The $f_{ex,0.5}^{GL}$, for most of the catalysts *(except the $Pd_{1000\_SA/NP}/CNT$ catalyst which contains a very low amount of metal)* is revealed to be high indicating a strong G-L mass transfer impact on the $STY_{0.5}$ measurements and the impossibility to discuss robustly these $STY_{0.5}$. This is indicated in the main text of the article. Interestingly, the 2 more active catalysts present a higher $STY_{0.5}$ compared to the theoretical STY^{max}. This is a phenomenon already observed and explained in stirred tank reactors with very active fine slurry catalyst particles [9, 10]. The approach detailed in [9] is very close to an enhancement factor, E (-), for mass transfer G-L reactive absorption already well established [11]. In the present work, this situation is encountered. Thus, the first points at a reaction progress of 0.5 are used to estimate an experimental E factor as shown in the 6th column of the table. The values are equal to 1 when $\boldsymbol{f_{ex,0.5}^{GL}}$ <100% and equal to the value of $\boldsymbol{f_{ex,0.5}^{GL}}$ when >100%. The values obtained here for the two more active catalysts are consistent with those reported in [9]. For the other reaction progress, accordingly to these measurements, the $F_{H2}^{max,GL}$ (and STY^{max}) takes into account this factor accordingly to (S9):

$$F_{H2}^{max,GL} = \boldsymbol{E} k_L a_{GL} V_R C_{H2}^* \quad \text{(S9)}$$

For reaction progresses of 2.0 and 2.5 $mol_{H2}/mol_{myrcene}$, the impact of G-L mass transfer on the STY is drastically decreased as shown in the Table and a satisfactory comparison of the observed STY can be drawn on a chemical basis. The Pd_{10SA_NP}/CNT, which is the most active one, is the only catalyst that may still present a possible partial G-L mass transfer hindrance of its intrinsic performance. This partial leveling is a signature of its very high intrinsic activity and does not change the conclusions made in this article. In a quantitative point of view, one can just expect an increase of the observed differences between this catalyst and the other ones.

S.4.2. L-S external mass transfer

In G-L-S slurry reactors, L-S external mass transfer is often less limiting than the G-L one. To verify this common assumption, the classical external mass transfer fraction, f_{ex}^{LS} (defined in S10) has been used for reaction progresses of 0.5, 2.0 and 2.5 $mol_{H2}/mol_{myrcene}$.

$$f_{ex}^{LS} = \frac{\overline{r_P} L}{k_S C_{H2}^*} = \frac{STY}{STY^{max,LS}} \quad \text{with} \quad STY^{max,LS} = \frac{M_{Pd} k_S C_{H2}^*}{\rho_P wt.\%_{Pd} L} \quad \text{(S10)}$$

L is the characteristic length of the catalyst (dp/6 for spherical particles) and k_S is the L-S mass transfer coefficient. It has been estimated using the correlation of Armenante & Kirwan [12]. The different results are presented in Supplementary Table 4:

Supplementary Table 4: Appraisal of L-S external mass transfer limitations.

Catalyst	$STY^{max,LS}$ ($mol_{H2}/s/mol_{Pd}$)	$STY_{0.5}$ ($mol_{H2}/s/mol_{Pd}$)	$f_{ex,0.5}^{LS}$ (-)	$STY_{2.0}$ ($mol_{H2}/s/mol_{Pd}$)	$f_{ex,2.0}^{LS}$ (-)	$STY_{2.5}$ ($mol_{H2}/s/mol_{Pd}$)	$f_{ex,2.5}^{LS}$ (-)
Pd/Al_2O_3	137	109	79%	10.2	7.5%	4.6	3.4%
Pd/C	541	168	31%	72	13.3%	26	4.8%
Pd/CNT **also named** $Pd_{2\ SA/NP}/CNT$	31 486	144	0.5%	44	0.1%	22	0.07%
$Pd_{1000\ SA/NP}/CNT$	642 309	184	0.03%	1.4	0.0002%	0.7	0.0001%
$Pd_{200\ SA/NP}/CNT$	48 294	104	0.2%	10.4	0.02%	4.5	0.01%
$Pd_{40\ SA/NP}/CNT$	46 884	544	1.2%	104	0.2%	50	0.1%
$Pd_{10\ SA/NP}/CNT$	49 791	672	1.4%	272	0.6%	106	0.2%

At a reaction progress of 0.5 $mol_{H2}/mol_{myrcene}$, only Pd/Al_2O_3 and Pd/C present a L-S mass transfer limitation. All the CNT catalysts appear free of external L-S mass transfer limitation.

At reaction progress of 2.0 and 2.5 mol/mol, no L-S mass transfer limitation remains at all for all the catalysts (except slightly for the Pd/C) and STY comparisons are consistent and chemically robust.

S.4.3. Internal mass transfer

To evaluate a possible internal mass transfer limitation, the classical Weisz-Prater criterion φ' [13] has been evaluated. When the criterion is inferior to 1 a surface efficiency of 1 is stated. When it is superior to 1, a surface efficiency is approximated as $1/\varphi'$The Supplementary Table 5 presents the results and equations (S11) to (S13), the formula used for .

$$\varphi' = \frac{\overline{r_p} L^2}{D_{eff} C_{H2,su}} \quad \text{(S11)}$$

$$D_{eff} = \frac{\beta_P}{\tau} D_{m,H2} \quad \text{(S12)}$$

For $\varphi' > 1$: $\eta_{su} \approx \frac{1}{\varphi'}$ and for $\varphi' < 1$: $\eta_{su} \approx 1$ (S13)

Supplementary Table 5: Appraisal of possible internal mass transfer limitations.

Catalyst	$Deff\ (m2/s)$	$STY_{2.0}$ ($mol_{H2}/s/mol_{Pd}$)	φ' (-)	η_{su} (-)	$STY_{2.5}$ ($mol_{H2}/s/mol_{Pd}$)	φ' (-)	η_{su} (-)
Pd/Al_2O_3	$4.0x10^{-10}$	10.2	2.10	≈0.5	4.6	0.95	≈1
Pd/C	$4.0x10^{-10}$	72	1.44	≈0.7	26	0.52	≈1
Pd/CNT **also named** $Pd_{2\ SA/NP}/CNT$	$1.4x10^{-9}$	44	0.004	1	22		1
$Pd_{1000\ SA/NP}/CNT$	$1.4x10^{-9}$	1.4	$1x10^{-5}$	1	0.7		1
$Pd_{200\ SA/NP}/CNT$	$1.4x10^{-9}$	10.4	$6x10^{-4}$	1	4.5		1
$Pd_{40\ SA/NP}/CNT$	$1.4x10^{-9}$	104	$6x10^{-3}$	1	50		1
$Pd_{10\ SA/NP}/CNT$	$1.4x10^{-9}$	272	0.015	1	106		1

All the CNT catalysts at reaction progress 2.0 and 2.5 $mol_{H2}/mol_{myrcene}$ are free of internal limitations. This remains true for the reference Pd/Al_2O_3 and Pd/C at the reaction progress of 2.5 $mol_{H2}/mol_{myrcene}$. For these catalysts, an intermediate regime with little mass transfer resistance may be present at a reaction progress of 2.0 $mol_{H2}/mol_{myrcene}$ because $1 < \varphi' < 3$. This is due to the bigger size of the catalyst particles.

S.4.4. Global conclusion on mass transfer limitations

Due to the high reactivity of the terminal alkene and the conjugated double bond of myrcene, the first hydrogenation is very fast and the overall hydrogenation of this study is subject to external mass transfer limitations (either G-L, L-S or both) at low reaction progress (typically < 1.0 $mol_{H2}/mol_{myrcene}$). For the usual reference hydrogenation catalysts (Pd/Al_2O_3 and Pd/C), at higher reaction progress, (2 or 2.5 $mol_{H2}/mol_{myrcene}$), most of the experimental instantaneous STY measurements are free of external or internal limitations. Only the most active catalysts ($Pd_{40\_SA/NP}$/CNT and $Pd_{10\_SA/NP}$/CNT) can be subject to a little G-L limitation that may hinder slightly their true performance.

Regarding internal mass transfer limitations, only Pd/Al_2O_3 and Pd/C may be subject to a little hindrance of their true kinetics at a reaction progress of 2.0 $mol_{H2}/mol_{myrcene}$. This latter tends to disappear at a reaction progress of 2.5 $mol_{H2}/mol_{myrcene}$.

Overall, comparison of instantaneous STY of this study is allowed and consistent for reaction progresses higher than 2.0. The conclusions drawn in this paper can be linked with chemical phenomena.

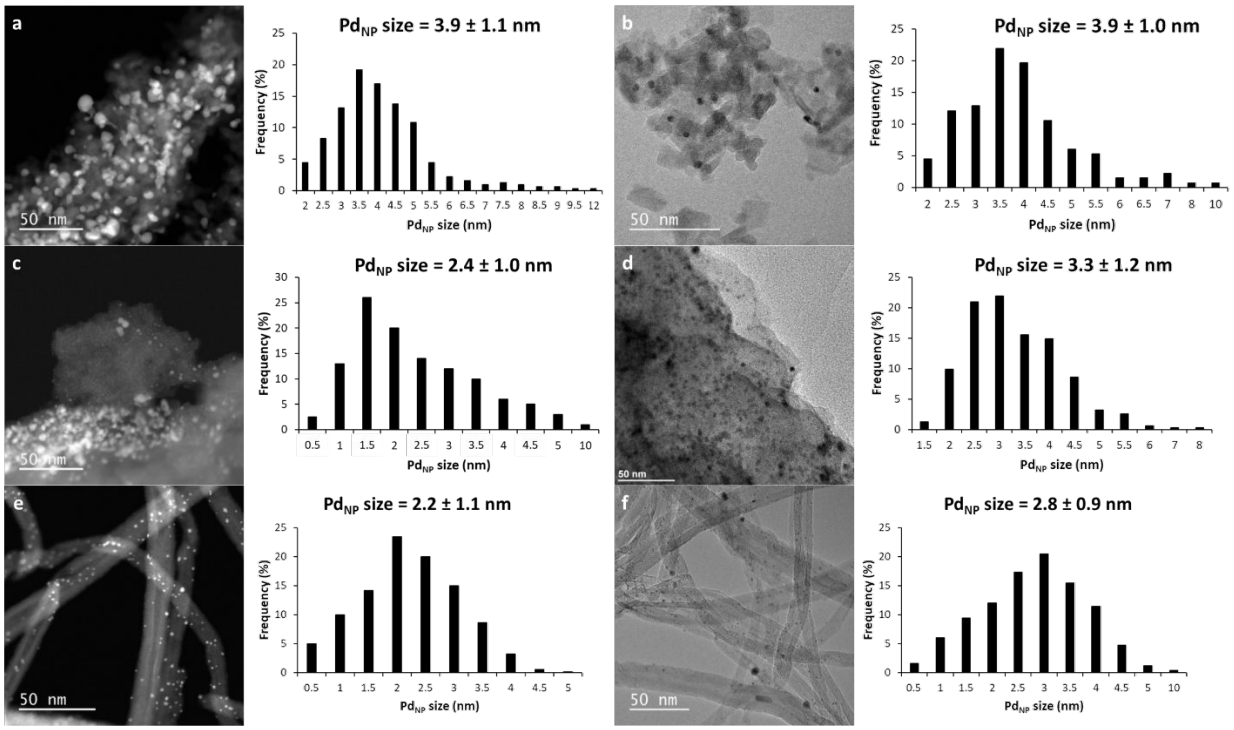

Fig. S1. STEM-HAADF and TEM micrographs, and histograms of Pd_{NP} sizes of: **a** fresh Pd/Al_2O_3; **b** Pd/Al_2O_3 after β-myrcene hydrogenation; **c** fresh Pd/C; **d** Pd/C after β-myrcene hydrogenation; **e** fresh Pd/CNT; and **f** Pd/CNT after *β*-myrcene hydrogenation. Scale bar = 50 nm.

Fig. S2. Photo of the metallic foam coated in the tubular reactor for catalyst stability study under continuous reactor operation.

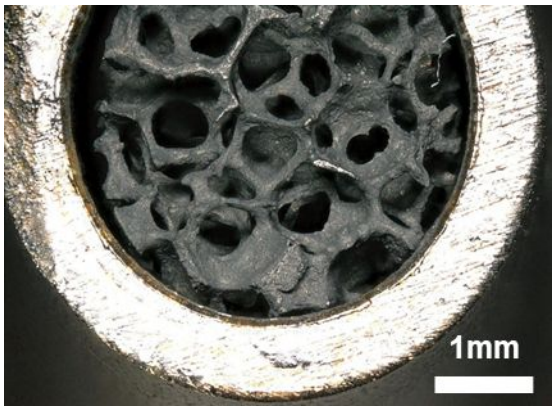

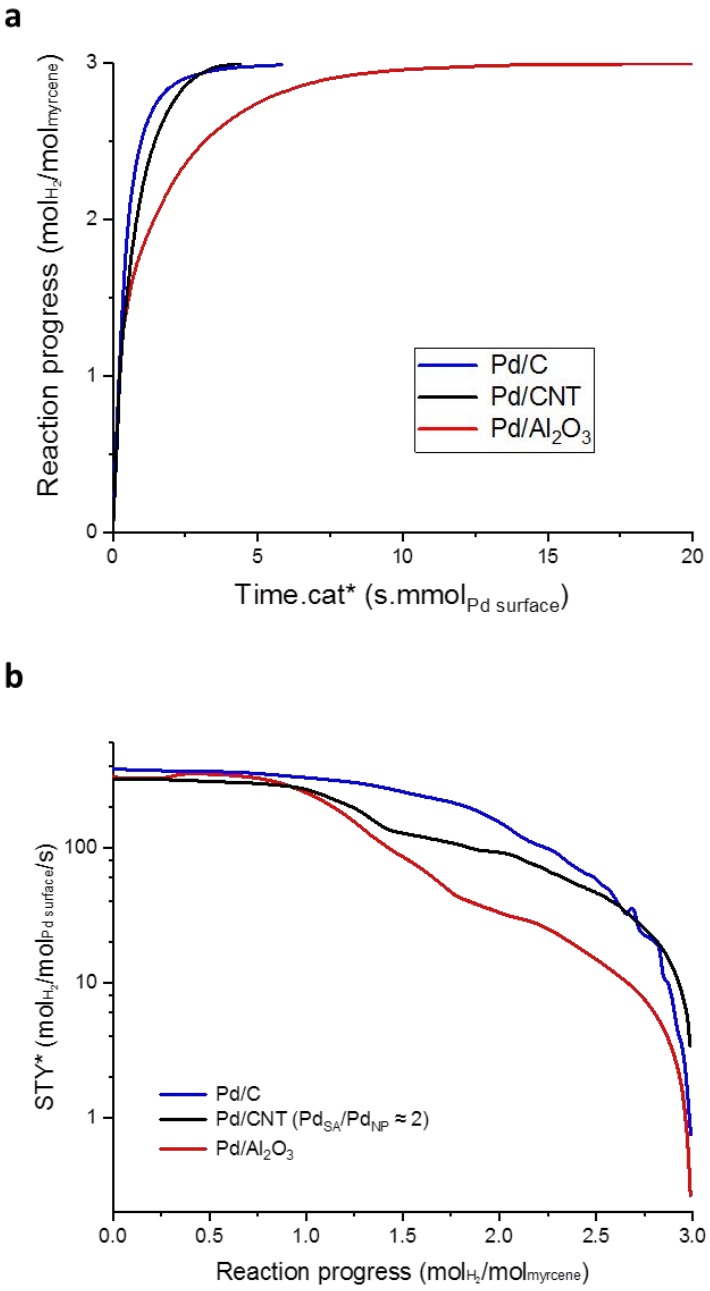

Fig. S3. Catalytic results on Pd/Al_2O_3, Pd/C and $Pd_{2\_SA/NP}$/CNT as a function of surface Pd. β-myrcene hydrogenation reaction. The reaction was carried out over supported Pd catalysts. P_{H2} = 20 bar - T = 120°C - myrcene 1 M (80 mL) - solvent heptane - 200 mg cat. **a** Reaction progress as a function of time.cat*. **b** STY* as a function of reaction progress.

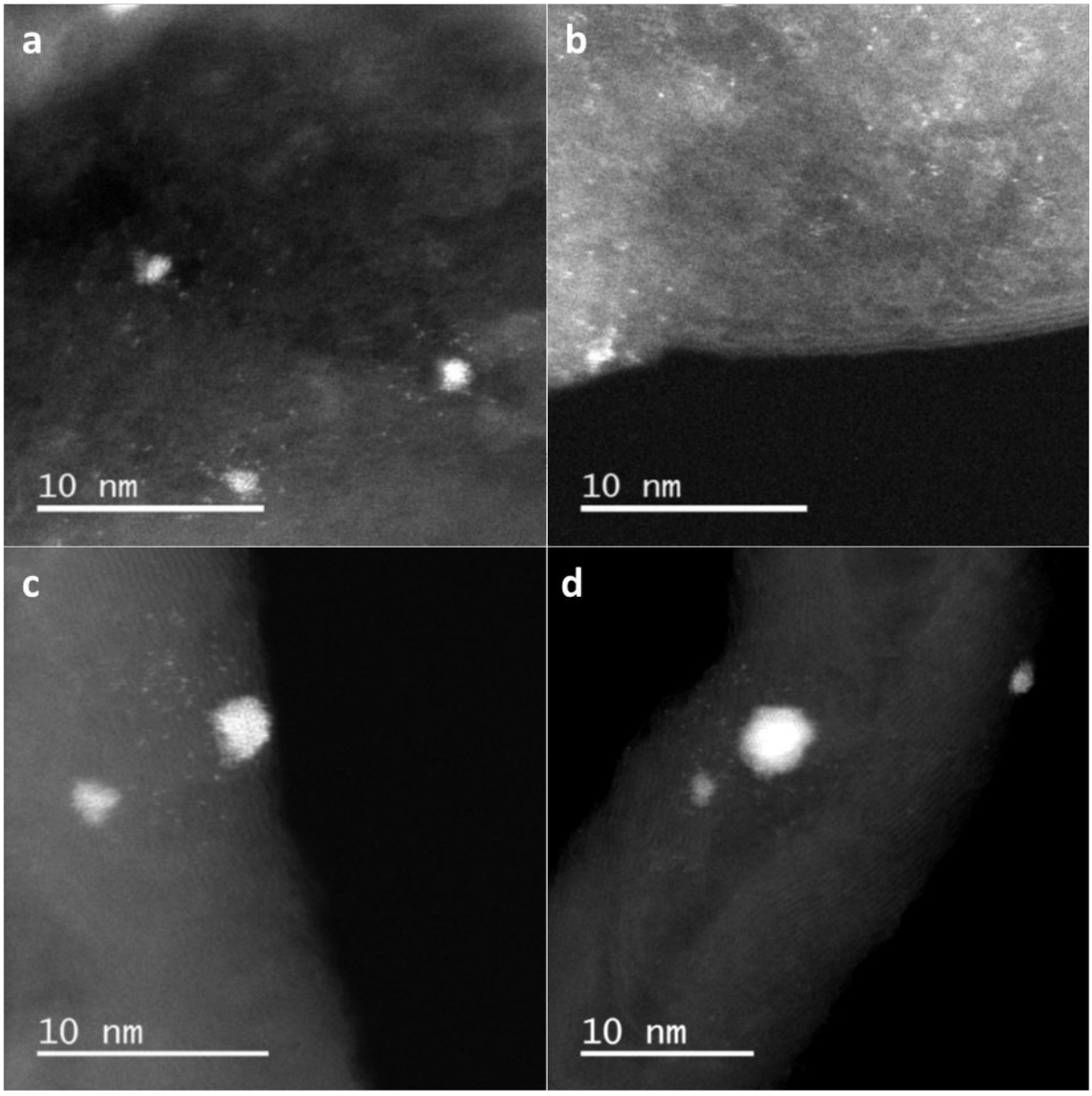

Fig. S4. STEM-HAADF images of **a** and **b** Pd/FLG (FLG = few layer graphene); and **c** and **d** Pd/CNF (CNF = carbon nanofibers), showing the coexistence of Pd SA and Pd NP.

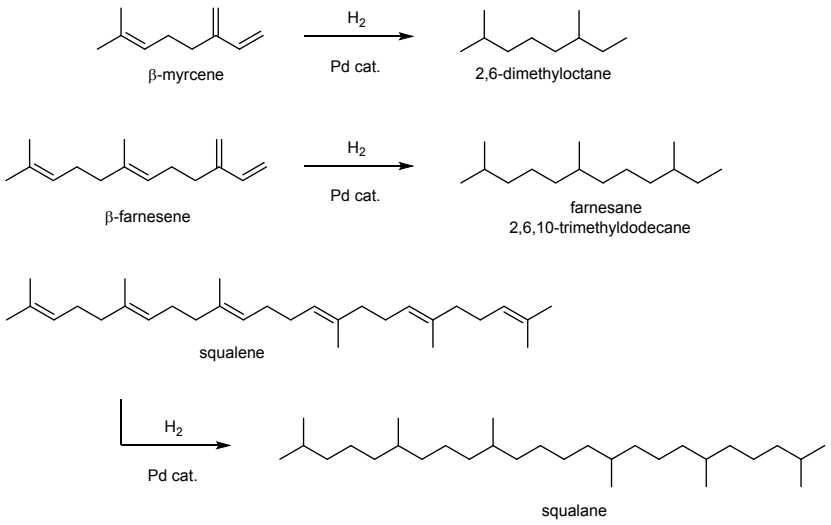

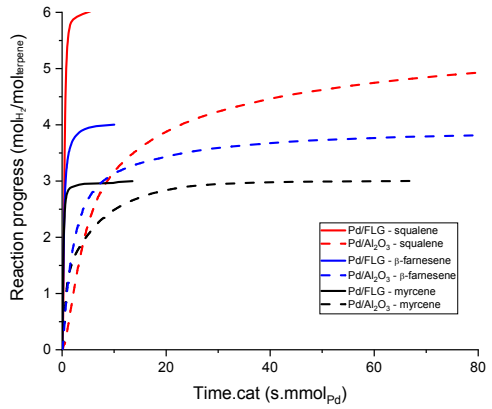

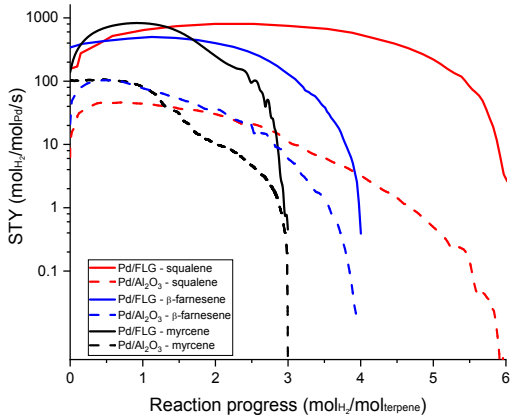

Fig. S5. Comparison of the catalytic performances of Pd/Al_2O_3 and Pd/FLG for the total hydrogenation of myrcene, farnesene and squalene. Hydrogenation reactions carried out over supported Pd catalysts. PH_2 = 20 bar - T = 120°C - substrate 1 M (80 mL) - solvent heptane - 280 mg cat.

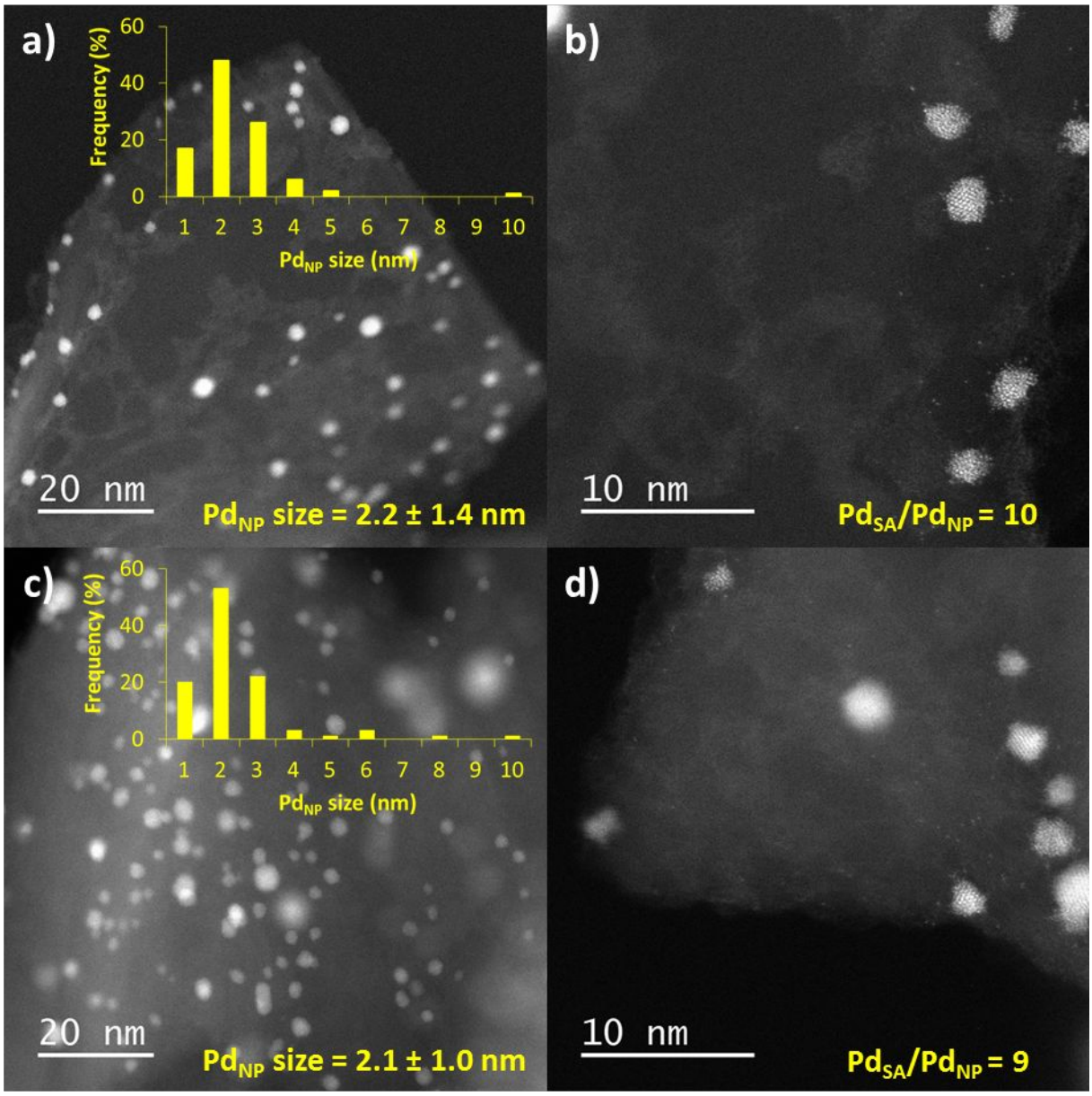

Fig. S6. STEM-HAADF micrographs, particle size distribution and Pd_{SA}/Pd_{NP} ratio for the Pd/FLG catalyst: a) and b) before catalysis; and c) and d) after myrcene hydrogenation.

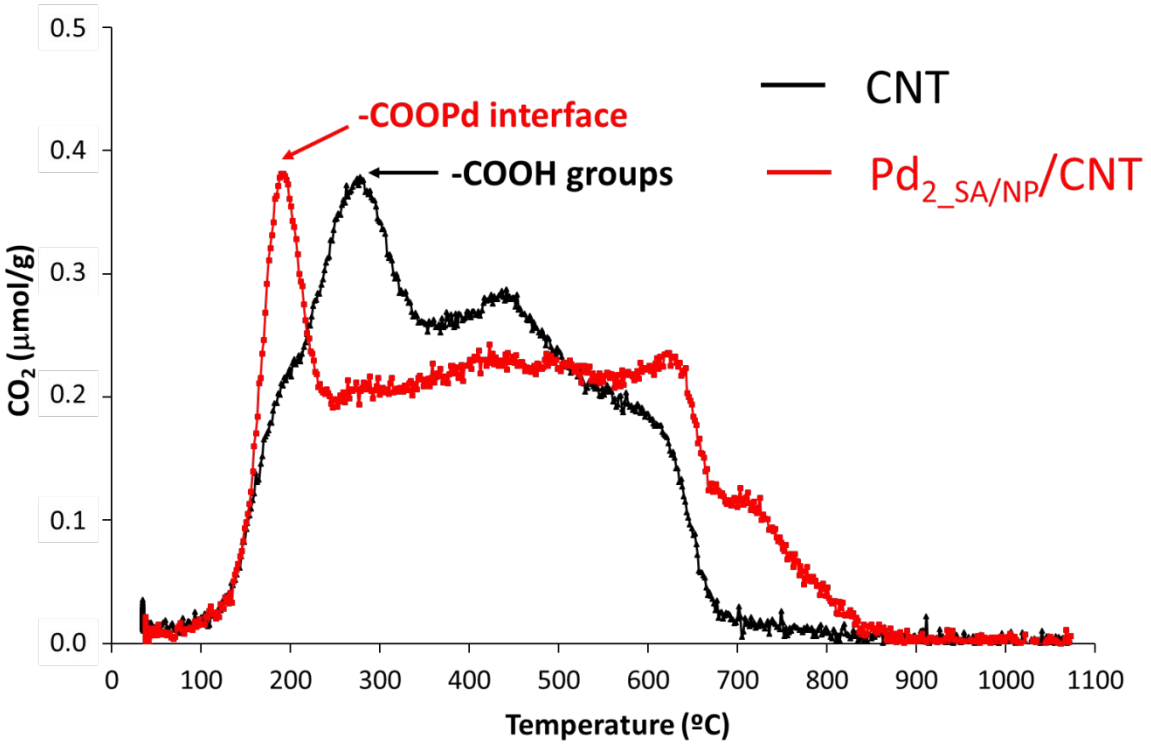

Fig. S7. CO_2 TPD profiles of the CNT support and the $Pd_{2\_SA/NP}$/CNT catalyst showing the disappearance of most of the surface carboxylic groups after catalyst preparation, and the appearance of a Pd-OOC- interface.

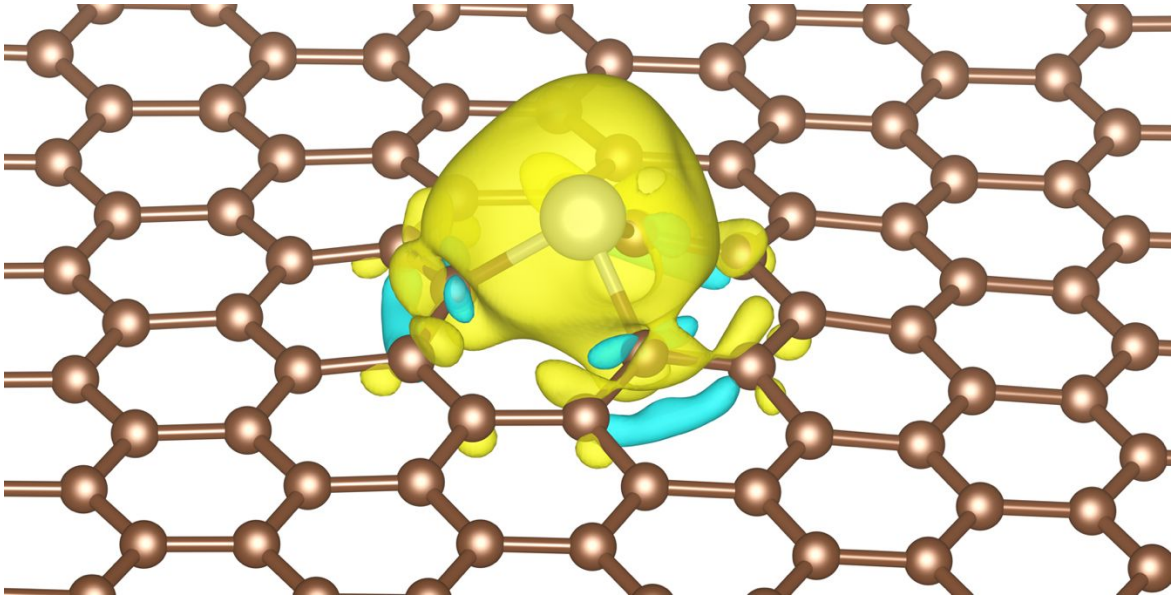

Fig. S8. Isosurface plot of the electronic density differences ($\Delta\boldsymbol{\rho} = \boldsymbol{\rho_{Pd-SAC}} - \boldsymbol{\rho_{Pd}} - \boldsymbol{\rho_{SAC}}$) for negative (in cyan) and positive (in yellow) isovalue of 0.002 e^-/Å. The charge transfer from Pd SA *4d* orbitals to the defective (single vacancy in graphene) support is estimated to be 0.37 e^-.

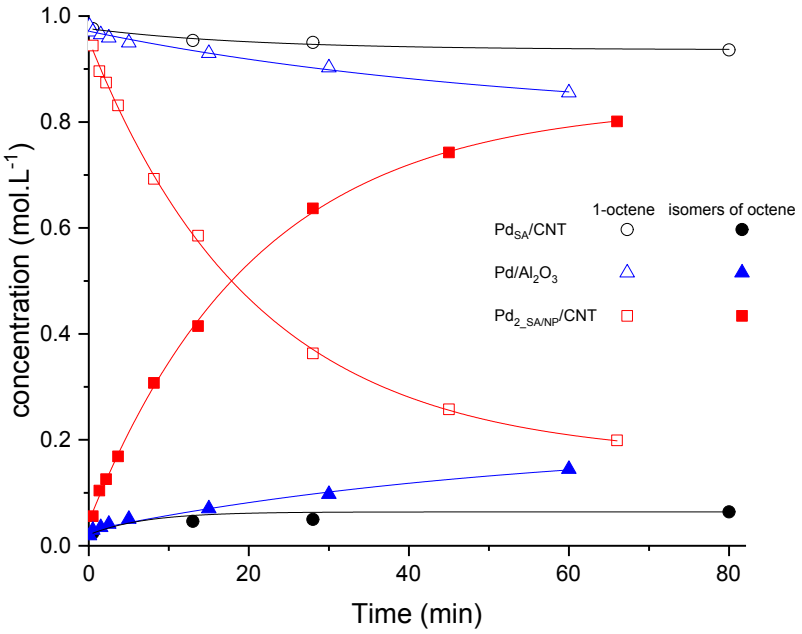

Fig. S9. Evolution of the composition of the solution during 1-octene hydrogenation as the function of time and catalysts Pd_{SA}/CNT, Pd/Al_2O_3 and $Pd_{2\_SA/NP}$/CNT. Reaction conditions: 1-octene (1M) in heptane, Pd 0.4 mg (60 ppm), reflux (98 °C), H_2 1 atm. In the case of the CNT catalyst no measurable activity was noticed.

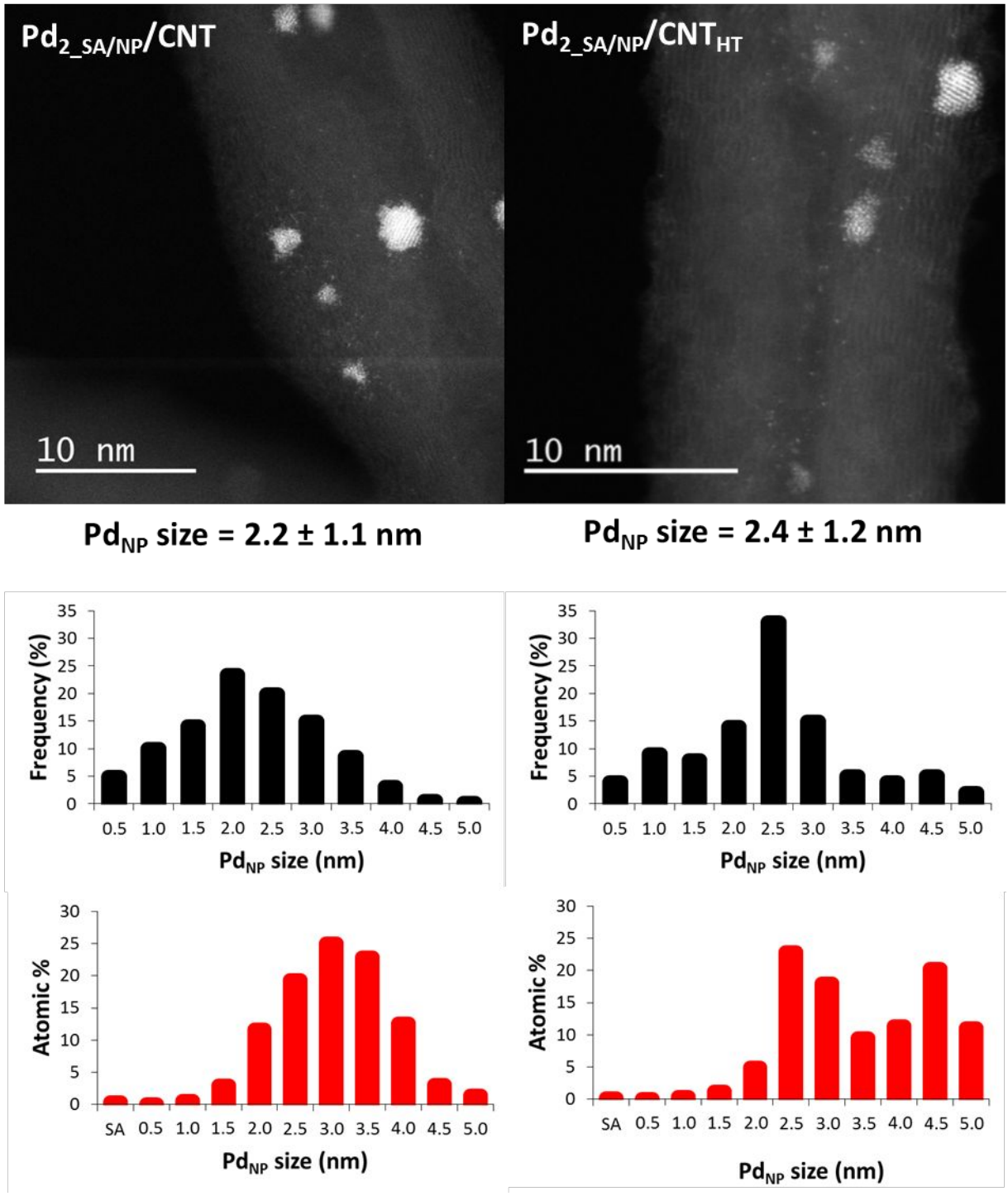

Fig. S10. STEM-HAADF micrographs of $Pd_{2\_SA/NP}/CNT$ and $Pd_{2\_SA/NP}/CNT_{HT}$ catalysts and related particle size distribution based on total particles and on total atoms.

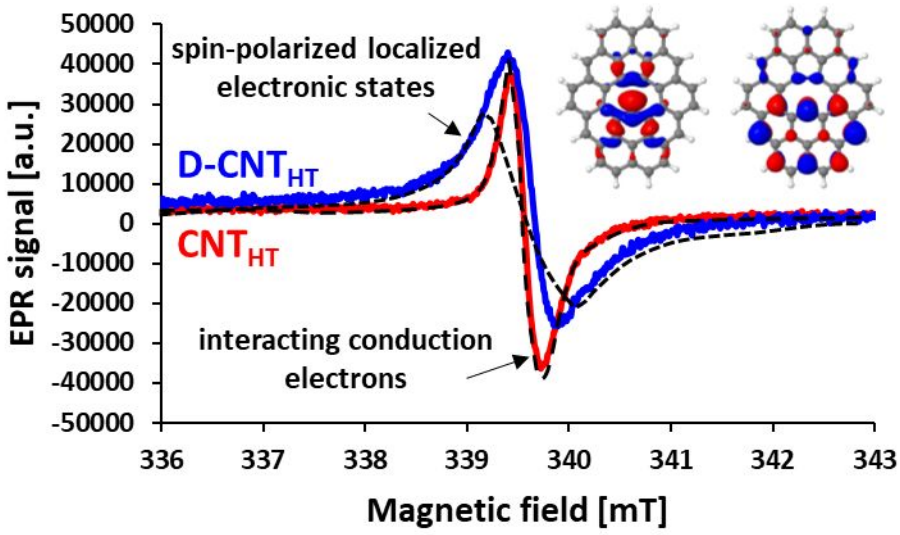

Fig. S11. EPR spectra of CNT_{HT} and D-CNT_{HT}. For these measurements, CNT have been heat-treated at 2800 °C before the thermochemical process in order to remove any traces of remaining metal arising from their synthesis.

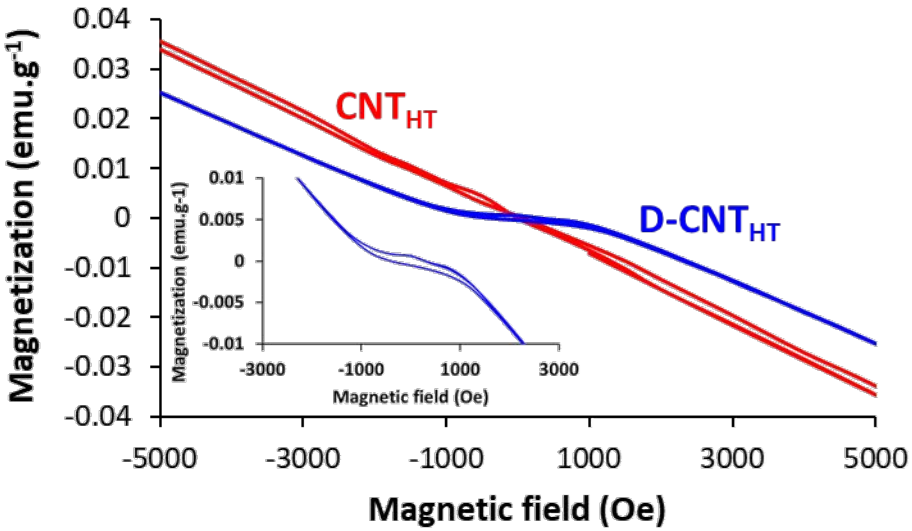

Fig. S12. VSM magnetization curves of CNT_{HT} and D-CNT_{HT}. For these measurements, CNT have been heat-treated at 2800 °C before the thermochemical process in order to remove any traces of remaining metal arising from their synthesis.

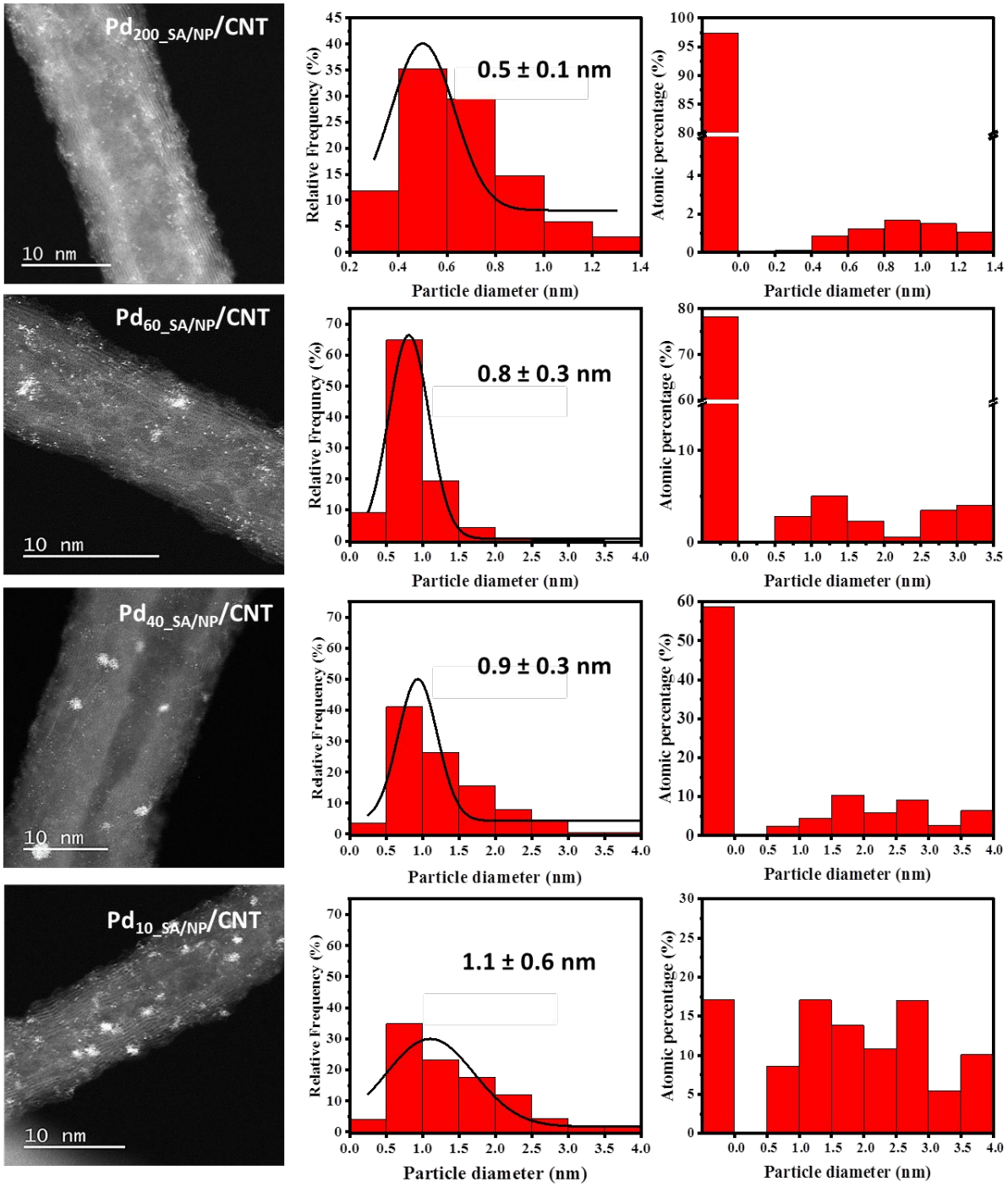

Fig. S13. STEM micrographs and particle size distribution based on total particles and on total atoms for $Pd_{200\_SA/NP}$/CNT, $Pd_{60\_SA/NP}$/CNT, $Pd_{40\_SA/NP}$/CNT and $Pd_{10\_SA/NP}$/CNT samples.

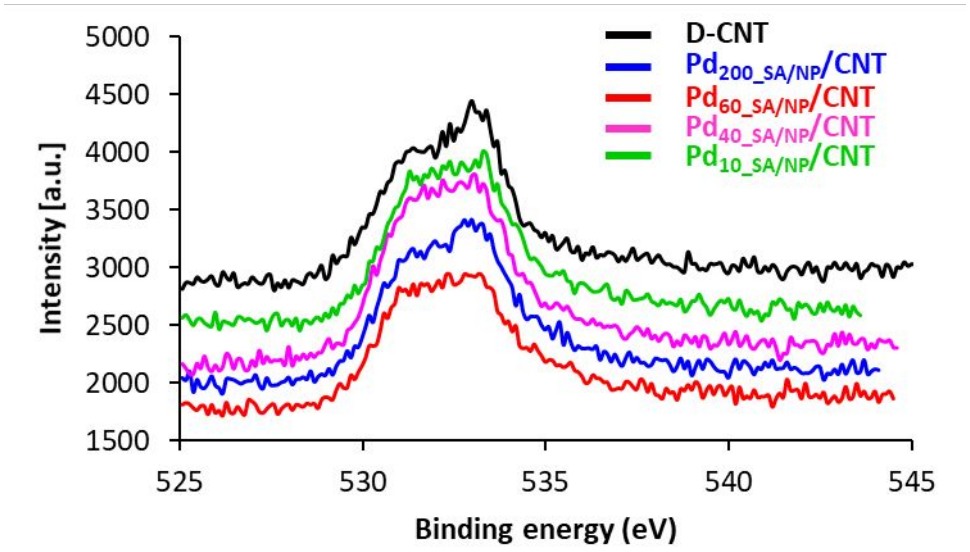

Fig. S14. O 1*s* XPS spectra of $Pd_{200\_SA/NP}$/CNT, $Pd_{60\_SA/NP}$/CNT, $Pd_{40\_SA/NP}$/CNT, $Pd_{10\_SA/NP}$/CNT and D-CNT.

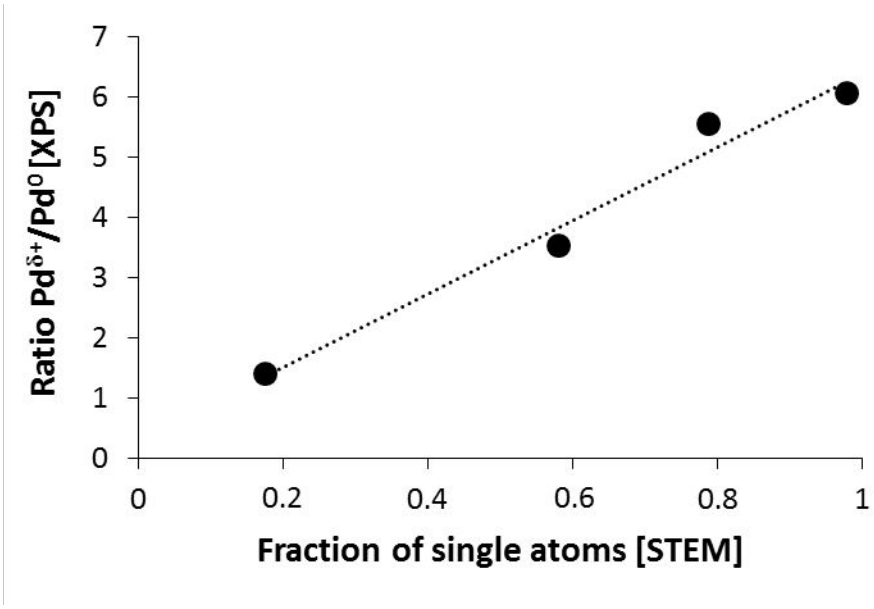

Fig. S15. Correlation between the ratio $Pd^0/Pd^{\delta+}$ determined by XPS and the fraction of SA in the same samples determined from STEM.

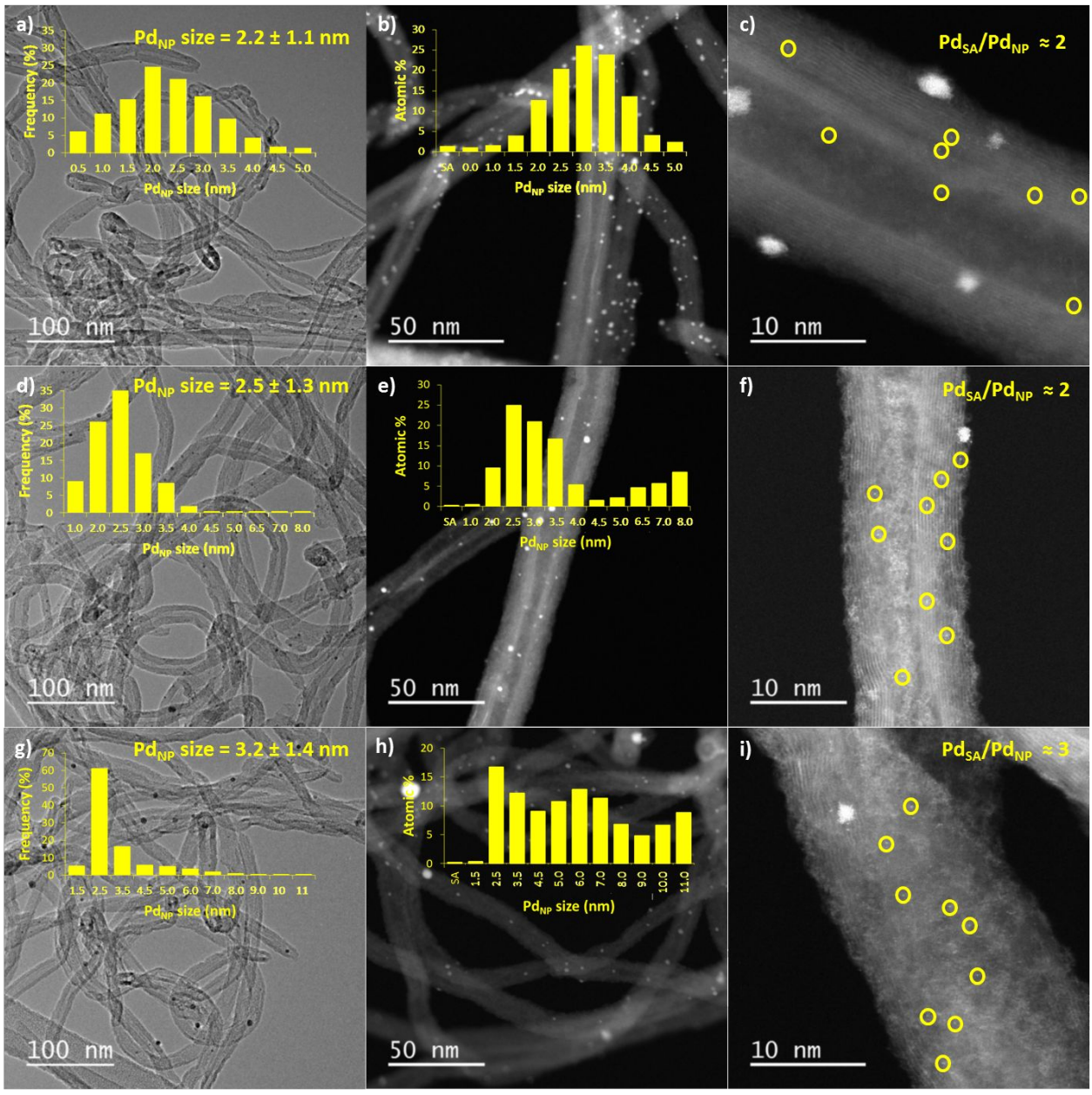

Fig. S16. TEM and STEM micrographs and particle size distribution based on total particles and on total atoms for: a) to c) $Pd_{2\_SA/NP}$/CNT; d) to f) $Pd_{2\_SA/NP}$/CNT coated on metallic open-cell solid foam cylinders before catalysis; and g) to i) $Pd_{2\_SA/NP}$/CNT coated on metallic open-cell solid foam cylinders after catalysis.

Additional references

1. A. Borodzinski, M. Bonarowska, Relation between crystallite size and dispersion on supported metal catalysts, Langmuir, 13 (1997) 5613-5620.
2. S. Khoobiar, Particle to particle migration of hydrogen atoms on platinum-alumina catalysts from particle to neighboring particles. J. Phys. Chem., 68 (1964) 411-412.
4. R. C. Reid, J. M. Prausnitz, B. E. Poling, The properties of gases and liquids 4th edition, McGraw-Hill Inc. New York (1987).
5. E. Lam, J. H. T. Luong, Carbon materials as catalyst supports and catalysts in the transformation of biomass to fuels and chemicals. ACS Catal. 4 (2014) 3393-3410.
6. S. Jin, W. Qian, Y. Liu, F. Wei, D. Wang, J. Zhang. Granulated carbon nanotubes as the catalyst support for Pt for the hydrogenation of nitrobenzene. Aust. J. Chem. 63 (2010) 131-134.
7. P. W. A. M. Wenmakers, J. van der Schaaf, B. F. M. Kuster, J. C. Schouten. ‘‘Hairy Foam’’: carbon nanofibers grown on solid carbon foam. A fully accessible, high surface area, graphitic catalyst support. J. Mater. Chem., 18 (2008) 2426-2436.
8. R. V.Chaudhari, R. V. Gholap, G. Emig, H. Hofman. Gas-Liquid mass transfer in dead-end autoclave reactors. Can.J. Chem. Eng. 65 (1987) 744-751.
9. E. Dietrich, C. Mathieu, H. Delmas, J. Jenck. Raney-Nickel catalyzed hydrogenations: gas-liquid mass transfer in gas-induced stirred slurry reactors. Chem. Eng. Sci. 47 (1992) 3597-3604.
10. Z. Junmei, X. Chunjian, Z. Ming. The mechanism model of gas-liquid mass transfer enhancement by fine catalyst particles. Chem. Eng. J. 120 (2006) 149-156.
11. S. Karve, V.A. Juvekar. Gas absorption into slurries containing fine catalyst particles. Chem. Eng. Sci. 45 (1990) 587-594.
12. G. F. Froment, K. B. Bischoff. Chemical Reactor Analysis and Design. Wiley, New York (1990).
13. P. M. Armenante, D. J. Kirwan. Mass transfer to microparticles in agitated systems. Chem. Eng. Sci. 44 (1989) 2781-2796.

Statement of contributions

Author contributions. P.S. conceived the idea of cooperative catalysis and coordinated the work. I.C.G. and I.R. performed the DFT calculations. C.R.C. prepared and characterized the mixtures of single atom catalysts and nanoparticles. B.G. and L. V. performed the catalytic experiments and GC-FID and GC-MS analyses. R.P., C.B. and A.F.R. conceived, supervised and analyzed the catalytic experiments. R.C.C. prepared and characterized the Pd catalysts. B.F.M. performed and analyze the TPD experiments.